A numerical and experimental study on a prototype "fish-friendly" water turbine swirl injector

by

Ajith Airody

A thesis
presented to the University of Waterloo
in fulfillment of the
thesis requirement for the degree of
Master of Applied Science
in
Mechanical and Mechatronics Engineering

Waterloo, Ontario, Canada, 2017

I hereby declare that I am the sole author of this thesis. This is a true copy of the thesis, including any required final revisions, as accepted by my examiners.

I understand that my thesis may be made electronically available to the public.

Abstract

The ever increasing demands for energy world-wide has prompted research into and implementation of devices to harvest power from renewable sources of energy, such as hydroelectricity. Large-scale hydroelectric plants have existed for over a century, and are capable of producing over 10000 MW of power. However, such facilities are expensive and generally have a significant impact on the local ecosystem; as such, there are relatively few locations and communities that can support their construction. Small-scale hydroelectric facilities, which produce power up to 30 MW, are increasing in popularity since they do not divert the natural flow of the river and are capable of harnessing energy from smaller sources than their large-scale cousins one of the main concerns being the negative effects they can have on the local fauna. Specifically, fish inadvertently passing through the facility can be hurt or killed by the inlet guide vanes or rotor assembly through a variety of mechanisms, including striking the structure, being caught between rotating and stationary parts, or through dramatic changes in fluid pressure.

In order to mitigate injury to fish passing through small-scale hydroelectric facilities, AlphaStar Hydro has developed a novel vaneless swirl injector to replace current inlet guide vane stages, which allows the fish to travel through with minimal damage, while still imparting the necessary swirl component onto the flow for proper turbine operation. This swirl injector is made up of a single spiral flighting wrapped around a central shaft. The main focus of this work is on quantifying and optimizing the flow through the vaneless swirl injector.

Of primary concern is the axisymmetry of the flow exiting the injector, the pressure drop across it, and the swirl that it provides, all of which directly impact rotor performance. Based upon a preliminary patented design provided by AlphaStar Hydro, the flow field generated by the injector was determined through a computational fluid dynamics study. This provided the foundation for a geometric optimization study to maximize flow axisymmetry and swirl, while minimizing pressure loss. A 5 by 4 grid was setup using number of revolutions and pitch angle as variables. Four metrics were measured: axial axisymmetry, tangential axisymmetry, swirl number and pressure loss. Using the four metrics, an objective function was created and was subsequently optimized using a line search algorithm. The study concluded that the number of revolutions is not as important as the pitch angle and that the optimal geometry is 4 revolutions at a pitch angle of 25 degrees.

A test rig was designed and constructed in order to test the newly optimized design with the addition of the nose cone. The setup is composed of a reservoir, a pump, a gate

valve, a circle-to-rectangle transition, flow conditioning elements, the swirl injector, a test section and return plumbing. The rig was commissioned and initially characterized by measuring the velocity drift with time, the change in temperature with time, and the inlet velocity profile upstream of the injector.

The experimental facility was coupled with numerical simulations to explore the flow field downstream of the optimized swirl injector with an attached nose cone, as would be the case upon rotor installation. The pressure, axial velocity and tangential velocity contours were analyzed to assess the performance of the swirl injector in its operational configuration, in preparation for rotor installation. A recirculation zone on the nose cone was observed, which was due to the flow separation on the nose cone. The swirl numbers and the axisymmetry metrics were compared between the optimization model and the nose cone model, revealing that there were no significant differences between the two. The experimentally measured velocity profiles were found to match well with the numerical profiles, as did the pressure distributions within the test section. This provided cross-validation of the experimental and numerical studies. The experimental data exhibited relatively high fluctuations in the velocity signals, however.

Dedication

This thesis is dedicated in the memory of A. Subramanya Karanth and Prof. G. Sridhara Rao.

Airody Ajja, your kindness, generosity and dedication to your family inspire me still.

Ajja Rao, your advice and amazing personality shaped who I am today. Also, you were right, I would have made a horrible architect!

Table of Contents

List of Tables

List of Figures

xiii

Nomenclature

α Blade exit angle (Chapter 1); Step size (Chapter 2)

$\bar{u}_i$ Time-averaged velocity component

β Planck constant

δ_{ij} Kronecker Delta

$\dot{m}$ Mass flow rate

η Efficiency of the turbine

Γ_m Average velocity torque

$\hat{P}$ Non-dimensional pressure

$\hat{u}_z$ Bulk velocity through pipe

∇ Gradient operator

ν Kinematic viscosity

Ω Rotor angular speed

Π Buckingham Pi non-dimensional variable

Ψ Pitch angle

ρ Density of fluid

θ Cylindrical coordinate θ

$\tilde{u}_i$ Fluctuation from average velocity (spacial)

$\tilde{u}'_i$	Average velocity (spacial)
C_w	Swirl velocity
D	Pipe diameter
d	Hub (inner tube) diameter
f	Dimensionless distribution function
g	Gravity
G_θ	Axial flux of angular momentum
G_z	Axial flux of axial momentum
H	Height (Chapter 1); Hessian matrix (Chapter 2)
K	Pressure loss coefficient
k_u	Dimensionless tip speed velocity
k_{V_m}	Dimensionless meridional velocity
L	Rifling length (Chapter 2); Inlet length variable (Chapter 3)
M	Mesh length
n	Number of revolutions of the rifling
P	Static pressure
p	Optimization direction
Q	Flow rate (Chapter 1); Objective function (Chapter 2)
r	Cylindrical coordinate r
Re	Reynolds number
S	Swirl number
U	Tip velocity
u'_i	Velocity fluctuation

u_i Velocity component

$u_{i,asymm}$ Asymmetry metric

$u_{i,T}$ True velocity

V_m Meridional velocity

x Cartesian coordinate x-axis

y Cartesian coordinate y-axis

z Cartesian coordinate z-axis

Chapter 1

Introduction

Hydroelectric energy is an attractive option for areas with numerous bodies of water. Traditionally, hydroelectric facilities are large-scale structures with high energy outputs. The cost of building and maintaining these large-scale structures, however, is also significant. On average, the capital cost of developing a hydroelectric site is $1B USD [1]. This cost includes the materials, transportation, and land development. There is also an environmental cost to developing these facilities: large-scale hydroelectric facilities often require the creation of large reservoirs which flood the surrounding areas, disturbing the local ecosystem, and displacing the local human and animal populations [1].

With increasing energy demands, the need for sustainable and renewable energy has increased [2, 3]. The lower head of small-scale turbines allows these facilities to be more versatile in terms of the water source, permitting otherwise neglected sources, such as small rivers and streams, to become viable energy producers [4, 5]. Small-scale facilities generally operate as "run-of-river" facilities, which means they operate without disrupting the natural flow of the river. In these facilities, a small portion of the river's flow is diverted to be used to run the facility. Furthermore, the support structures for the facility are used only to regulate the flow at the intake and cause very little disruption to the surrounding ecosystem [6]. Small-scale hydro-electric facilities have a lower cost and reduced impact on the environment, making them an attractive alternative to the large-scale facilities. They also naturally have a lower energy output, usually with a maximum cap of 2.5 to 30 MW, due to the lower operational head. Facilities with less than 2 MW output can be classified in sub-categories such as mini- (500 kW to 2 MW), micro- (less than 500 kW) and pico-hydro (less than 10 kW) [4, 6, 7, 8, 9, 10]. In this study, we will consider components of facilities in the mini- to pico- range.

Despite the fact that small-scale hydroelectric facilities significantly reduce the impact on the environment, fish drawn into the turbine can still be hurt or killed. Further details on the damage done to the fish drawn into the turbine will be discussed in later sections. In order to mitigate some of the damage done by inlet guide vanes (IGVs) and the rotor, AlfaStar Hydro has designed a vaneless casing, which replaces the traditional IGV array, coupled with a fish-friendly Kaplan turbine. The vaneless casing mimics the IGV array by creating the required swirl velocity component necessary for the runner by guiding the flow through a spiral-shaped track. The coupled casing and the runner assembly is presented in Fig. 2.1a. The lack of vanes reduces the fish mortality caused by strike damage dramatically [11].

The primary issue with the current casing design is that the flow field exiting the injector tends to be less axisymmetric than that produced by traditional IGVs, thus reducing the efficiency of runners developed for the turbine. Herein, a combined numerical and experimental study is performed to characterize and optimize the design of the vaneless swirl injector for use in small-scale turbine facilities. The numerical study focuses on reforming the geometry of the injector by varying two parameters and optimizing several flow characteristics in order to obtain the superlative configuration. The experimental investigation focused on the design and characterization of the experimental setup as well as the validation of the numerical results.

1.1 Background

In this section, background information on types of water turbines and hydro-electric facilities will be given. The design and operation of inlet guide vanes and rotors will also be discussed as well as the dangers of turbine operation for the fauna going through the facility.

1.1.1 Hydro-electric facilities

Both large- and small-scale hydroelectric facilities are composed of similar parts. The main difference between the two types of facilities is the presence of the dam for the large-scale facilities. The main interior components of a hydroelectric facility are the intake, the penstock, the IGV array, the turbine, the draft tube, and the tail race (see Fig. 1.1).

The intake is where the flow initially enters the facility. There is also usually a trash rack to stop large debris from entering the facility and damaging the IGVs or the rotor. In
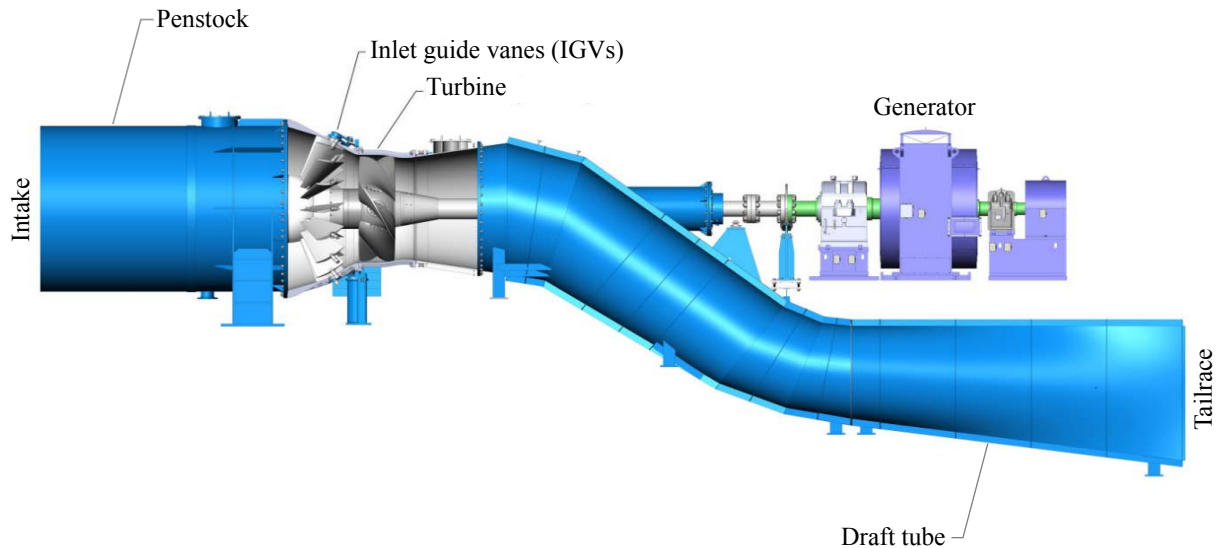
Figure 1.1: Components of an axial flow water turbine facility. Adapted from a figure courtesy of NORCAN Hydraulic Turbine Inc. [12]

some of the larger facilities, there are also flow control gates at the intake used to control the flow velocity through the turbine.

The design of the intake is crucial to the proper operation of the system. Specifically, the design of the weir is critical to the smooth operation of the facility. If a river bed has a lot of gravel, the weir can become filled, at which point any intakes upstream will ingest a lot of debris. This debris can badly damage the turbine over time and result in a deterioration of the tubine performance. The solution for this particular problem is the installation of a streambed weir. A streambed weir functions by making the water crest over the weir and then be funneled into an intake, therefore stopping most of the gravel from entering the intake.

After entering the intake, the flow then passes through the penstock. Penstocks are made of different materials depending on the application. The most common materials are steel and plastic, though wood is also used on occasion. Steel penstocks are the most common type. They are manufactured in fixed length segments, which are then welded or bolted together on site.

The penstock directs the flow to the inlet guide vanes. The IGVs are used to give the incoming flow a circumferential velocity component, which is necessary in order to effectively extract energy with the rotor. In smaller facilities, the IGVs are also used to regulate the flow through the turbine. IGVs are present in most turbine facilities, with the

exception being Pelton wheel type facilities [13].

The rotor (or runner) is the heart of the facility since the rotor is what extracts the energy from the flow. The rotor converts the energy of the flow into mechanical energy in the form of a rotating shaft, which is, in turn, converted to electrical energy by connecting to a generator.

After the flow goes through the rotor, it passes through the draft tube. The draft tube is effectively a diffuser designed to recover a portion of the pressure head. The flow coming out of the rotor is at a high velocity and relatively low pressure. Without the draft tube, there can be backflow into the exit. Due to the draft tube, the pressure is increased at the outflow, stopping the backflow [13, 14]. The design of the draft tube is especially important for low head turbines since as much as 7 m of head can be recovered through proper draft tube design.

While the design of the draft tube varies from project to project, there are a couple of standard practices. Firstly, a straight conical section of the draft tube is required for at least one rotor diameter downstream of the runner. Some draft tubes have a 90 degree bend in them. The bend needs to be designed such that there is a slight contraction as it bends, which improves efficiency by minimizing flow separation and reversal [13].

Finally, the flow exits the facility through the tailrace, which returns the water to the river.

1.1.2   Types of water turbines

There exists a multitude of water turbine designs for a variety of applications and geographical conditions. Turbines are divided into two main classes: impulse and reaction turbines. The most common impulse turbines are the Pelton, Turgo, and Cross-flow types. The most common reaction turbines are the Kaplan and Francis designs [15, 16].

Impulse turbines

Impulse turbines operate by using the kinetic energy of the water to drive the rotor. The flow subsequently discharges to the atmosphere. The runners are in air and are driven by the water jets.

The Pelton turbine works by having a high speed jet impinge on the buckets located on a rotating wheel. The impinging jet is split in two as it hits the buckets and each half-jet is deflected almost 180 degrees [16, 17]. The energy extracted is solely the kinetic energy

of the incoming flow. Pelton turbines are usually used in locations with high elevations. Generally, they are found in locations with total head greater than 300 m. The main advantages of Pelton turbines are that they can accommodate water laden with silt and that the blades are easy to repair [15].

Turgo turbines are similar to the Pelton turbines but have a different bucket shape. The impinging jet also comes in at an angle. By having the jet impinge at an angle, the flow travels from one side of the bucket to the other eliminating the negative interactions between the discharge flows from different buckets. This allows the Turgo turbines to be built with a smaller diameter than the Pelton while maintaining the power output [16, 17].
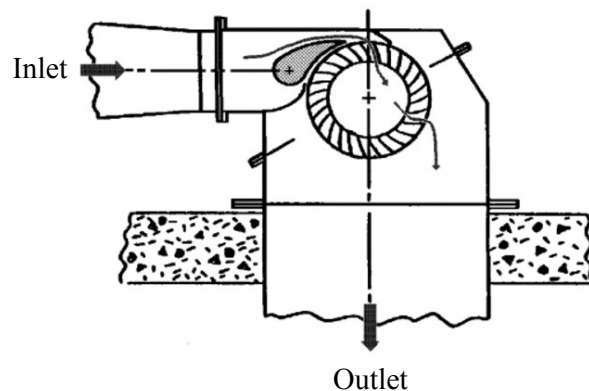
Figure 1.2: Diagram of cross-flow turbine adapted from Paish et al.[18]

The Banki or cross-flow turbines operate similar to traditional water wheels. The water jet impinges upon the wide buckets on one side of the runner and exit on the other side (see Fig. 1.2). The nozzle for the cross-flow turbines are wider than the nozzles for the Turgo and Pelton turbines in order to accommodate for the wider blades. The main advantages of the cross-flow design is that it is cheaper than the other impulse turbine and is capable of taking larger flows at lower heads. They are also more versatile than their counterparts since they can operate over a larger range (see Fig. 1.3). The main disadvantage is that the Banki turbine is less efficient than the Turgo or Pelton turbines [16, 17].

Reaction turbines

Reaction turbines generate electricity by converting both the pressure energy and the energy contained in the moving water. Unlike impulse turbines, reaction turbines have their rotors completely submerged. This class of turbines is generally used at lower head, higher flow rate locations [16].

5
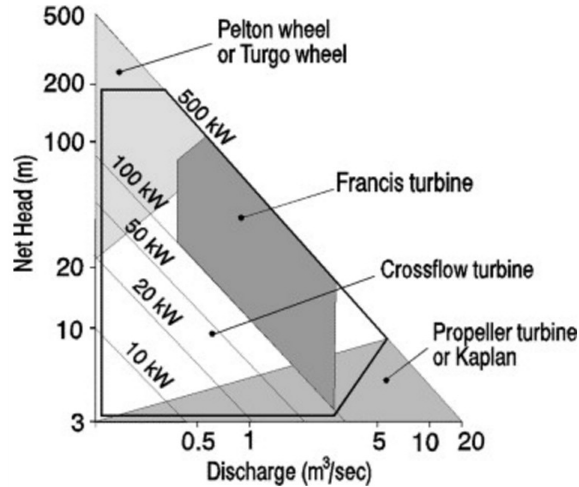
Figure 1.3: Operational ranges of different turbine designs [18].

The first radial inflow turbine was invented by James B. Francis [19]. The flow enters through a row of adjustable inlet guide vanes located right before the runners. Francis turbine are used in locations with a head of about 10 to 100 m. The rotors are shaped to perform optimally at a specific speed (i.e., a specific flow rate and head level). The turbine is placed vertically with the draft tube located at the bottom of the turbine [15, 19].

As the demand for power increased throughout the early 20th century, the need for a turbine that could be operated at small head levels (3 to 9 m) was recognized [19]. This is when inventor Viktor Kaplan proposed the Kaplan turbine. Modeled after a ship's propeller, this turbine is able to provide enormous amounts of power with very low head. More recently, the design of the Kaplan, has been improved by the addition of rotating blades [15, 19]. This allows for a greater flexibility and improved efficiency depending on the flow conditions. Presently, Kaplan turbines are used in large power-plant installations with total head between 20 to 70 m [15].

1.1.3   Inlet guide vane and rotor design and performance

The performance and proper design of IGVs are crucial in the proper performance of the rotor. The IGV array is what gives the flow its pre-swirl, the energy of which can then be extracted by the turbine. The design of the IGVs is dependant on the performance characteristics of the turbine [20].

There exists a multitude of guide vane designs depending on the application. Many of the 2D designs, such as the semi-circle [21], s-cambered, and tandem designs, are used as a simpler alternative to the 3D design [22]. What follows is a method for designing 3D guide vanes.

The three main variables of any turbine design are: the flow rate (Q), the available head (H) and the rotor angular speed (Ω). Generally, by knowing one of the three variables (usually H) the other two can be calculated by using the dimensionless values for the tip speed velocity (k_U) and the meridional velocity (k_{V_m}) (as seen in Eq. (1.1) and (1.2) in terms H). The values of (k_U) and (k_{V_m}) are obtained empirically from the accumulated experiences of various turbine manufacturers.

$$k_U = U/(2gH)^{1/2} \tag{1.1}$$

$$k_{V_m} = V_m/(2gH)^{1/2} \tag{1.2}$$

where U is tip velocity of the runner and V_m is the meridional velocity component. Based on the design variables, the required radial distribution of angular momentum at exit of the IGVs (which is the same as the radial distribution at the inlet section of the rotor) can be obtained [23].

Once the angular momentum distribution is determined, the streamline curvature method is used to determine the meridional velocity profiles between the blades and on the surface of the blades [23]. Using the meridional velocity distributions, the velocity triangles (and the subsequent angle relationships between velocity components) at the exit edge of the guide vane can be determined. The exit blade angle for the average meridional streamline ($\alpha_{2,m}$), as well as the average velocity torque (Γ_m), is determined. By assuming a uniform velocity torque at the outlet of the guide vane, the rest of the exit angles (α_2) along the edge can be determined:

$$r \cdot \cot(\alpha_2) = \Gamma_m \tag{1.3}$$

The equation is based on a 2D Euler analysis, and therefore does not represent the full flow. The equation is only used for the design of the blades. The guide vane inlet angles (α_1) are usually set to 90 degrees (from the radial axis) in order to accommodate

7

the incoming flow which is assumed to be axial. With the inlet and outlet angles, the rest of the angles along the meridional streamlines can be determined:

$$\alpha = \alpha_{1,i} + f_i(l) \cdot \Delta\alpha \tag{1.4}$$

where $f_i(l)$ is a dimensionless distribution function and $\Delta\alpha = \alpha_2 - \alpha_1$. The subscript i denotes the different streamlines.

In most designs the thickness of the guide vanes is kept constant, with exception to the leading and trailing edges. The leading edge is usually rounded out (mimicking a NACA airfoil) and the trailing is chamfered in order to prevent flow separation [23, 24].

The performance of the IGVs is often determined by the efficiency of the turbine as a whole (i.e., the combination of the IGVs and the rotor). The performance of IGVs can also be assessed from the pressure loss across the vanes. The pressure loss criteria is often used to analyze IGV designs for centrifugal pumps, where the pressure loss can cause there to be flow recirculation, and consequently a loss of pump performance [22].

The overall efficiency of the turbine (which includes the hydraulic and mechanical efficiency as a whole) is defined as the ratio between the net power extracted by the turbine and the maximum theoretical power [25]:

$$\eta = \frac{P_{net}}{P_t} \tag{1.5}$$

The theoretical power can be defined in two ways. The most common way is by defining it as a function of H and Q as,

$$P_t = \rho g H Q \tag{1.6}$$

Alternatively, the maximum power output can be defined by the 2D ideal flow Euler turbine equation (see Eq. (1.7)). Euler's equation requires an understanding of the velocity fields before and after the rotor, and therefore is not as convenient as the first method.

$$P_t = \dot{m} U (C_{w1} - C_{w2}) \tag{1.7}$$

where $\dot{m}$ is the mass flow rate, C_{w1} and C_{w2} are the swirl velocities at the inlet and outlet of the rotor, respectively.

In most cases, the inclusion of inlet guide vanes increases the performance of the turbomachine. The IGVs improve the pressure distribution before the flow encounters the rotor. They also ensure that the incoming flow's velocity vector match the angle of the rotor's leading edge [24, 26].

1.1.4 Scaling of the swirl injector

In order to scale the injector, the Buckingham Pi theorem is used to determine non-dimensional numbers which can be used to compare different sized swirl injector. It should be noted that this dimensional analysis is assuming that the general geometry of the injector stays constant (i.e. there is no change in the number of revolutions in the flighting or in the inlet angle) and only the diameter of the pipe is scaled. The main variables in swirl injector operation are the flow rate (Q), the available pressure ($P = \rho g H$), the pipe diameter (D), the density (ρ), and the viscosity (μ). The repeating variables are D, Q, and ρ. The following two variables were obtained:

$$\Pi_1 = \Pi_1(D, Q, \rho, P) \tag{1.8}$$

$$\Pi_2 = \Pi_2(D, Q, \rho, \mu) \tag{1.9}$$

By determining the coefficients for each of the variables in Π_1 and Π_2, the following formulations are found:

$$\Pi_1 = \frac{D^4 P}{Q^2 \rho} \tag{1.10}$$

$$\Pi_2 = \frac{D \mu}{Q \rho} \tag{1.11}$$

By observing the two non-dimensional variables, it can be seen that Π_1 is more useful than Π_2 since Π_1 contains the pressure term. Using Π_1, a direct comparison can be made between the test model and the scaled model:

$$\left(\frac{D^4 P}{Q^2 \rho}\right)_{\text{test}} = \left(\frac{D^4 P}{Q^2 \rho}\right)_{\text{scaled}} \tag{1.12}$$

By assuming that ρ and gravity stay constant, Eq. 1.12 can be simplified to:

$$\left(\frac{D^4 H}{Q^2}\right)_{\text{test}} = \left(\frac{D^4 H}{Q^2}\right)_{\text{scaled}} \tag{1.13}$$

Using Eq. 1.13, the swirl injector can be scaled up or down by matching the ratios. The scaled injector should have similar characteristics to the tested model. In order to match the scaled injector to a rotor, the rotor angular speed is adjusted to match the flow rate and available head.

1.1.5   Hazards for fauna caused by turbine operations

The repercussions of turbine use in rivers and estuaries can be seen when analyzing the survival rates of the fish that unwittingly pass through the turbines. In large-scale hydroelectric facilities, the survival rate of the fish navigating through the facility is about 70% [27]. In small-scale hydroelectric facilities the survival rate is 80-98% [27, 28]. Though there is high survival rate amongst the fish that travel through small-scale facilities, there are still mortalities linked (directly and indirectly) to their passage through the turbine and the associated structures. The mortality rate for small-scale facilities increases significantly when the facilities are placed in series [27, 28].

Čada has performed an extensive survey of all the factors that cause fish mortality or injury when passing through the turbine [29, 30]. The main causes of injury are the following: rapid and extreme pressure changes, cavitation, shear stress, turbulence, striking, and grinding. The injuries listed are caused by the different components of the turbine [29]. The survey was done for large-scale turbines, but since the parts for small-scale turbines are identical to their larger counterparts, it can be assumed that the same hazards are present in both cases, though not necessarily in the same order of significance.

The main hazard before the runner are the inlet guide vanes. The fish are prone to striking the IGVs, which can kill them instantly. If the initial strike does not kill the fish, the internal injuries can cause a delayed mortality [29]. The same injuries occur if the fish

10

hit the runner. The number and severity of the injuries depend on the number of blades, the speed at which the blades rotate, and the spacing between the blades [31]. The other hazard is the shear stress caused by the difference in velocity between the incoming flow and the flow past the guide vanes.

Between the runner blades, the fish are also susceptible to striking. They can also be injured by grinding against the area between the hub and the blade. Lastly, the fish can be subject to tremendous pressure changes. This is particularly true in turbines that have many short blades. The shorter the blade, the more abrupt and violent the change in pressure [11]. There is also damaging shear stress in between the blades [30].

Finally, when the fish are in the draft tube they are subjected to turbulence and cavitation. Cavitation is the formation of bubbles due to low water pressure. The low water pressure is found in the core of the helical vortex in the draft tube. This vortex originates from the swirling flow exiting rotor [32]. These bubbles subsequently collapse, hurting the fish. Turbulence in the outflow doesn't necessarily harm the fish directly but makes them disoriented, which leaves them vulnerable to predators as they exit the tail race. There is also extreme shear stress in this region [29, 30].

Among the fatalities and injuries seen in the passage through the turbine, there are certain physiological and physical factors which are common amongst the victims. The main physiological trait which influences the rate and frequency of injuries is the length of the fish. In a study done by Alden Laboratory in 2001 and 2002, it was found that 100% of the smaller eels were able to navigate through their testing turbine without injury versus the 99% of the larger eels [31].

Another common point is the orientation of the incoming fish. Depending on the orientation, even smaller fish can be struck. The orientation also has an effect on the severity of the shear stress induced injuries. It was shown in an experimental study done by Deng et al. that the fish which were oriented with their back towards an incoming jet suffered tremendous injuries due to their physiological disposition [33, 34].

1.2   Current state of the art

There have been many innovations in recent years regarding the design of small-scale water turbine facilities as well as the design of the rotor itself. This section focuses on the innovations regarding turbines on the lower end of the operational range (mini- to pico-hydro facilities).

1.2.1 Innovations in small-scale water turbines

Maintaining turbine performance with varying flow conditions is important to be able to sustain the required energy output. Turbines operate at maximum efficiency when the water flow is above 80% of the maximum flow rate seen by the turbine [35]. If the flow rate dips too low, there can be mechanical shocks and instabilities in the flow [35]. A solution to the problem of variable flow rates is to have two parallel turbines operating either in tandem or one at a time. The optimization for this solution was investigated by Anagnostopoulos et al. [36]. The results of this study are that, depending on the flow conditions, it is better to operate either one or both turbines with the size ratio of the turbines being between 0.4 - 0.5. Another solution is to continuously vary the speed of the turbine by means of a control system which regulates the governor (also known as a speed limiter). The speed is varied depending on the flow conditions which, based on the region, vary greatly depending on the season. In a study by Pérez et al., the implementation of a neural network in order to continuously control the speed of the rotor was investigated. By continuously varying the speed of the turbine in order to accommodate for the change in flow rate, the turbine's efficiency is maintained [37].

Modifications to the other parts of the facility also result in an improvement in cost and efficiency. It has been shown that having a larger diameter penstock can greatly reduce the head loss due to pipe friction in pico-hydro applications. Furthermore, since tubes come in standard diameters, increasing the diameter is a simple and inexpensive way of increasing the available head for the turbine. The reduction in price is especially important since it makes small-scale water turbines affordable to developing countries and rural communities [38, 39].

There have also been advances in the selection of turbine designs. Multi-criteria evaluations of different turbine designs has brought to light previously unknown applications for certain turbine types. In an article by Williamson et al. [40], it was shown that Turgo turbines, which were previously thought to be only useful in medium to high head applications, can be used in facilities with low head. While propeller-type turbines are still the best option for heads between 0.5 - 1.5 m, Turgo turbines can compete for heads above 1.5 m [40].

Many of the recent articles on the optimization of the turbine facilities recommend that IGVs be removed. These are largely focused on the facilities on the lower range of small-scale turbine (i.e., mini hydro facilities with 1.5 to 2 meters of head), where the exclusion of the IGVs has a minimal impact on the performance of the facility. In a study done by Singh et al. [41], it is recommended not to use IGVs in order to make the free vortex design paradigm described in the article feasible. In other studies, the guide vanes are eliminated

in order to prevent clogging. In these cases, the facilities are meant to run at one speed, hence the drop in performance is not as significant as turbines which are operating over a large range of speeds [25]. Often, the main reason for excluding the guide vanes is to make the facility more affordable [35].

Finally, one of the most important advances in small-scale water turbines is the emergence of novel blade designs and applications. A novel application is the addition of vertical axis turbine to water pipelines (see Figure 1.4). The facilities in a study by Chen et al. generate enough energy to power the instrumentation used to regulate the pipelines. The rotor is also a novel design, which is optimized for the flow conditions seen by a vertical turbine in a pipeline [42]. Another design for the vertical turbine is based off of a three-bladed wind turbine, designed to operate in channels [43]. Another design involves the use of the filament winding method in order to design and manufacture a novel rotor. The rotor was initially intended to be used as an axial compressor in water refrigeration systems [44].
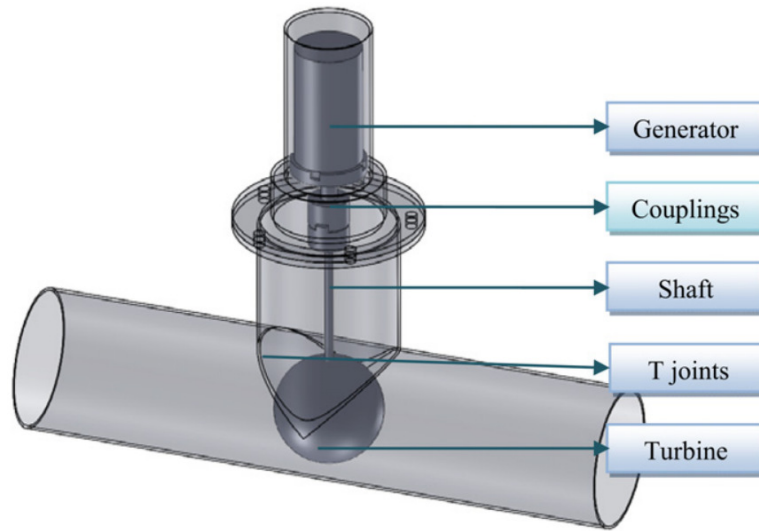
Figure 1.4: Diagram of a vertical turbine installation [42].

Recently, the applications of the rotor have changed from pumping to energy extraction. Winding impellers (as seen in Fig. 1.5) are advantageous due to the light-weight nature of the composite materials used in the fabrication. They also have a minimum impact on the fauna in the river system since the fish can travel through the middle of the rotor, hence avoiding the blades [45, 46].

13
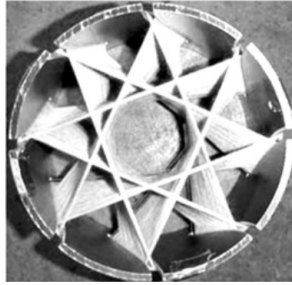
Figure 1.5: Rotor fabricated using the winding method [45].

1.2.2 Advancements and innovations in the fish-friendly turbine industry

The ongoing problem with fish fatalities requires new innovations from the industry. There have been significant advances in terms of the modeling of the risks and turbine design.

In terms of modeling, the main advances have been in the strike prediction and shear stress modeling. The modeling of strike is important in order to predict where the fish will be struck and with what probability. So far this has been mainly based on the works of Turnpenny et al. [47, 48, 49]. The Turnpenny model is based on ratio between the length of the fish and the spacing between the rotor blades. Essentially, if the fish was of a certain length, the probability was constant for a certain rotor. But their model was lacking a stochastic element in terms of the orientation. This is where Deng et al. (2007) implemented their stochastic model based off of the deterministic model proposed by Turnpenny et al. When compared to experimental results the stochastic model was much closer than its deterministic counterpart [34].

For stress modeling, a CFD model of the system is created and the subsequent stresses are evaluated for the different portions of the system. It should be noted that this method is not effective to predict the fatalities caused by the shear stress. The model is used more for comparison and as a modeling paradigm for future prototypes [30].

In turbine design, the main innovations have been in the runner design itself. The runners that are currently being developed by companies such as Alden and AlfaStar Hydro are a new breed of high reaction runners, which have fewer and longer blades than their competitors. Fewer blades reduces the risk of strike injuries and the longer blades allow for less abrupt pressure changes. Furthermore, there is virtually no gap between the blade and casing. This reduces the chance of grinding injuries significantly [11, 31]. Another innovation which is currently used in retrofitted hydro dams, is the minimum

gap runner (MGR). MGR turbines have a reduced gap between the hub and the blade by introducing a spherical design for the hub [29].

Efforts have also been made in order to reduce the strike injuries in the inlet. Some of these efforts have been done by AlfaStar Hydro with their vaneless casing which removes inlet guide vanes, hence reducing the risk of strike related injuries [11].

1.3   Proposed study and objectives

Herein we examine the swirl injector numerically and experimentally in order to elucidate the flow through the injector as well as the optimal geometry of the injector. Chapter 2 focuses on design optimization of the swirl injector with the objective being to find the optimal geometry of the swirl injector. Chapters 3 and 4 consider the incorporation of the optimized injector into a flow facility, wherein a cone is attached at the end of the injector at the eventual location of the rotor. The impact of the nose cone is explored numerically and experimentally, with the experimentally facility development presented in Chapter 3, and the results of the numerical and experimental studies in Chapter 4. Chapter 5 contains the conclusions derived from the study. Finally, recommendations for future studies are made in Chapter 6.

Chapter 2

Numerical optimization of a vaneless swirl injector[1]

In this chapter we numerically investigate the flow development within the vaneless casing in an effort to improve the overall component performance. Specifically, the impact of rifling pitch and length of the swirl injector on the exiting flow axisymmetry, swirl number, and pressure loss through the device is parametrically studied. An objective function consisting of weighted contributions from these performance measures is developed to aid in optimization of the injector design geometry. Recommendations for the design of the next generation vaneless fish-friendly swirl injector are developed based upon the optimization study.

2.1   Problem definition

Herein, we investigate the flow field within a vaneless swirl injector casing, shown in Fig. 2.1a upstream of an axial flow water turbine rotor. The analysis is performed absent of the runner, however. The effects of the runner and injector combination will be investigated in a future study. The casing comprises the inlet duct and rifling, which is shown schematically in Fig. 2.1b. A Cartesian coordinate system is defined with the origin located at the downstream end of the rifling, oriented such that the z axis is along the

---

[1]The contents of this chapter are being reviewed for publication in the Journal of Fluids Engineering. Professor Sean D. Peterson and David De Montmorency provided feedback and direction throughout the project.
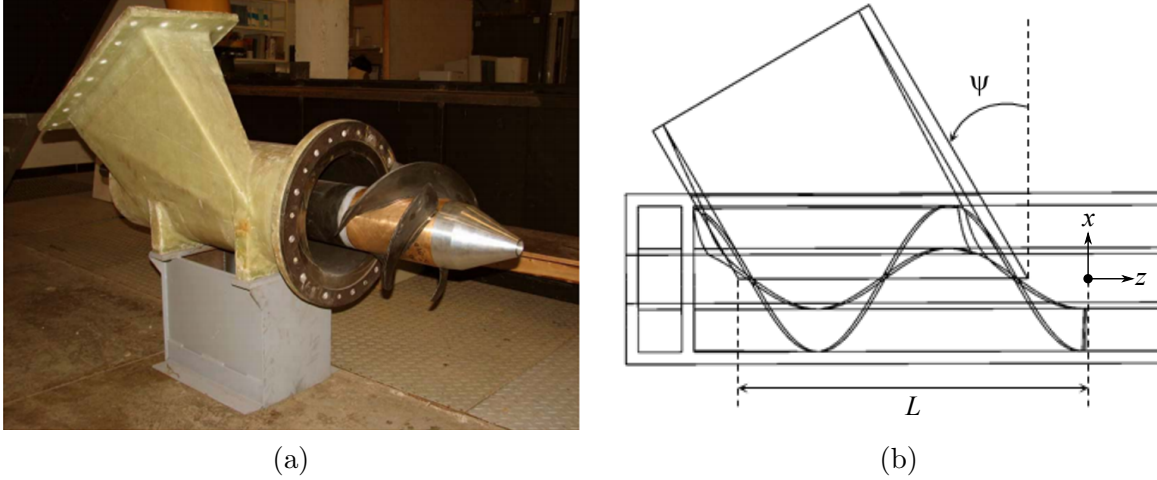
Figure 2.1: (a) Image of the vaneless casing and runner assembly developed by AlfaStar Hydro and (b) schematic of the casing with analysis variable definitions.

turbine axis of rotation, the x axis is oriented in the direction opposite to the gravitational vector $\mathbf{g}$, and the y axis is defined to form a standard right-handed coordinate system. At a given z plane, a local polar coordinate system is also defined, with r representing the radial coordinate and θ indicating the polar angle.

A rotor shaft collar of diameter d is aligned coaxially with the main flow pipe of diameter D. The inlet duct feeding the swirl injector has a rectangular cross-section with dimensions L by $(D-d)/2$ and is oriented at an angle Ψ with respect to the vertical (x) axis, see Fig. 2.1b. The duct interfaces with the annular pipe such that wider of the the parallel walls are tangent to the inner and outer annulus cylinders. This interface forms the start of the rifling, which accordingly has lead angle Ψ. The lead (or pitch) of the rifling is $L = \pi D \tan \Psi$. The total number of revolutions of the rifling is given as n.

The working fluid is water with density ρ and kinematic viscosity ν. The flow is assumed incompressible, steady, and Newtonian, and thus is governed by the Navier-Stokes equations. The flow in the casing is highly turbulent, and thus, to facilitate the solution of the Navier-Stokes equations, we employ the Reynolds decomposition, $u_i = \bar{u}_i + u'_i$, where $\bar{u}$ is the time-averaged velocity component, u' is the fluctuating velocity component, and subscript i indicates the spatial direction of the component using standard index notation [50]. Employing the Reynolds decomposition and averaging over time yields the Reynolds

17

Averaged Navier-Stokes (RANS) equations as

$$\frac{\partial \bar{u}_i}{\partial x_i} = 0 \tag{2.1}$$

$$\bar{u}_i \frac{\partial \bar{u}_j}{\partial x_i} = \frac{\partial}{\partial x_i} \left[\nu \left(\frac{\partial \bar{u}_i}{\partial x_j} + \frac{\partial \bar{u}_j}{\partial x_i} \right) - \frac{\bar{p}}{\rho} \delta_{ij} - \overline{u_i' u_j'} \right] \tag{2.2}$$

where $\bar{p}$ is the time averaged pressure, $\overline{u_i' u_j'}$ is the Reynolds stress tensor, ∇ is the gradient operator, and the Kronecker Delta $\delta_{ij} = 1$ for $i = j$ and 0 otherwise. In order to close this set of equation, the Reynolds stresses are modeled using the k-ω shear stress transport (k-ω SST) model, which tends to perform better than order closure models for swirling flows with a strong axial velocity components [51, 52].

2.1.1 Numerical model

The modeled turbine casing geometry is set at $d = 0.0635\,\text{m}$ and $D = 0.1524\,\text{m}$, with $\Psi = \{10°, 25°, 40°, 55°\}$ and $n = \{1, 2, 3, 4, 5\}$. The gauge pressure at the inlet plane is assumed constant at $31.55\,\text{kPa}$, which corresponds to $3.23\,\text{m}$ of head. The working fluid is water with density $\rho = 1000\,\text{kg m}^{-3}$ and kinematic viscosity $\nu = 1.004 \times 10^{-6}\,\text{m}^2\,\text{s}^{-1}$. The Reynolds number varies with Ψ and n, but is on the order of Re $\sim 10^6$. The outlet is a zero average pressure boundary, and the walls are no-slip.

The physical domain is discretized using the ANSYS ICEM module into primarily hexahedral elements with tetrahedral elements at the tip of the blade to accommodate the irregular geometry of the casing at this location, as shown in Fig. 2.2. An inflation layer is used along the walls of the model in order to resolve the velocity gradients in the boundary layer. In addition, the interface between the tip of the blade and the beginning of the radially symmetric section of the model has a higher mesh density due to the anticipated higher velocity gradients in this region. Beyond the tip of the blade the mesh is radially symmetric. The total number of elements increases with increasing Ψ and n, but is generally on the order of 6 million total elements.

Equations (2.1) and (2.2) are discretized using a second-order high resolution scheme and the k-ω SST model is used to model the Reynolds stresses. The governing equations are solved numerically using ANSYS CFX 15.0.

A mesh independence study was conducted with $n = 3$ for all values of Ψ by comparing axial and circumferential velocity profiles along a radial line at $\theta = 180°$ at several locations along the length of the draft tube (0, 0.5, 1, and $D2$ downstream of the swirl vane).
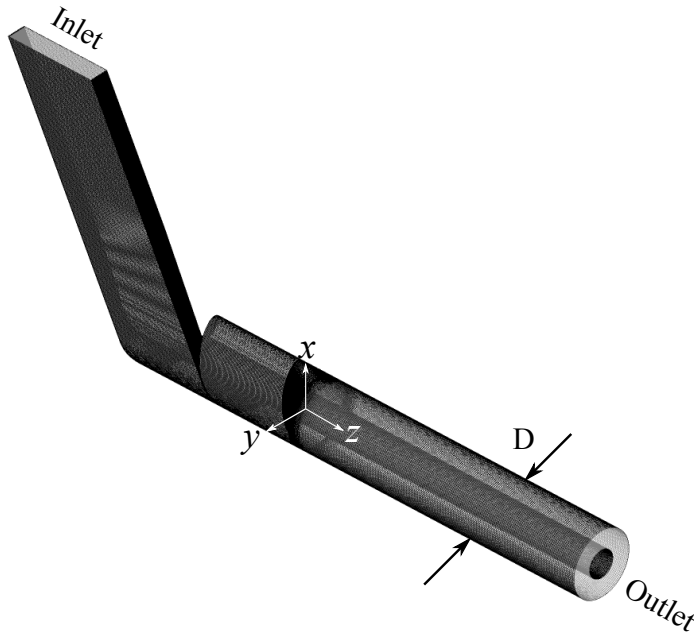
Figure 2.2: Isometric view of the full computational domain.

The mesh was considered converged when the average difference between velocity profiles for successive meshes was less than 5%. The converged mesh density was subsequently employed for the remainder of the models at the given pitch angle.

All combinations of Ψ and n are tested parametrically, as shown in the test matrix presented in Table 2.1. For the remainder of the document, shorthand notation will be employed to refer to specific test cases, as shown in Table 2.1. The notation concatenates n and Ψ as N(n)P(Ψ); that is, the N1P10 case has $n = 1$ and $\Psi = 10$.

2.1.2   Data analysis

Of primary interest for assessing the performance of the swirl injector are the velocity and pressure fields at $z/D = 0.5$; that is, $0.5D$ downstream of the tip of the rifling. This location is of particular interest as it is where the runner will be placed in the actual device. From the velocity and pressure fields we can assess important performance metrics, such as the axisymmetry of the flow at the location of the runner, the pressure loss through the system, and the fluid momentum in the axial and circumferential directions.

Most critical for runner design is axisymmetric flow fields at the runner location. Thus,

Table 2.1: Test case matrix.

n \ Ψ	10	25	40	55
1	N1P10	N1P25	N1P40	N1P55
2	N2P10	N2P25	N2P40	N2P55
3	N3P10	N3P25	N3P40	N3P55
4	N4P10	N4P25	N4P40	N4P55
5	N5P10	N5P25	N5P40	N5P55

we develop a metric for assessing the axisymmetry of both the axial and circumferential velocity fields at various cross-sections downstream of the rifling. We first consider the circumferentially averaged velocity in a z-plane, defined as

$$\tilde{u}_i(r, z) = \frac{1}{2\pi} \int_0^{2\pi} u_i(r, \theta, z) \ d\theta \tag{2.3}$$

where the subscript i indicates the particular velocity component of interest (axial or circumferential). This yields a nominal velocity profile in the given z-plane to enable assessment of the axisymmetry. Deviation from the mean is obtained from the root mean square, as

$$\tilde{u}_i'(r, z) = \left[\frac{1}{2\pi} \int_0^{2\pi} (u_i(r, \theta, z) - \tilde{u}_i(r, z))^2 \ d\theta \right]^{\frac{1}{2}} \tag{2.4}$$

A measure of the total asymmetry in a given plane is then obtained by averaging the deviations in Eqn. 2.4 over the radius as

$$u_{i,\text{asymm}}(z) = \frac{2}{D} \int_0^{D/2} \tilde{u}_i'(r, z) \ dr \tag{2.5}$$

In practice, discrete approximations of Eqns. 2.3-2.5 are employed by extracting data from 45 equally radially spaced concentric circles, each consisting of 200 discrete points equally spaced in the θ direction. Using these discrete data, the integrals in these equations are replaced with summations.

While axisymmetry of the flow at the rotor plane is important for rotor design and efficiency, the overall energy available for extraction is related to the relative momentum in the circumferential and axial directions. This is captured in the dimensionless swirl

number, which is the ratio of the axial flux of angular momentum G_θ to the axial flux of axial momentum G_z defined as [53, 54]

$$S = \frac{2G_\theta}{DG_z} \tag{2.6}$$

The momentum fluxes are defined as

$$G_\theta = \int_A \rho r u_\theta u_z \; \mathrm{d}A \tag{2.7}$$

$$G_z = \int_A \rho u_z^2 \; \mathrm{d}A \tag{2.8}$$

where u_θ is the circumferential velocity and u_z is the axial velocity.

Lastly, we consider the pressure loss through the injector as a performance metric, as this has a direct impact on the energy available for extraction, with higher losses meaning less available energy. The pressure loss through the injector is defined as the difference in average pressure between the inlet P_i and the rotor plane P_t. That is,

$$\Delta P = \hat{P}_i - \hat{P}_t \tag{2.9}$$

where a hat indicates an area average, that is $\hat{\{\cdot\}} = (1/A) \int_A \{\cdot\} \; \mathrm{d}A$, where A is the cross-sectional area.

For the remainder of the manuscript, all variables will be presented in nondimensional form, unless otherwise noted. Specifically, D will be employed as the length scale, the average axial velocity $\hat{u}_z$ will be used as the velocity scale, and the pressure will be normalized by $\rho \hat{u}_z^2$.

2.2 Flow results

2.2.1 General observations

In order to properly visualize the flow development through the casing, a representative case is selected. The N2P25 case is selected since it is near the middle of the testing domain. Figure 2.3 shows the streamlines of the N2P25 test case from the inlet to the outlet. The rifling geometry is included for clarity. The streamlines enter the flow domain and proceed along a straight path until encountering the rifling, at which point the fluid begins to flow
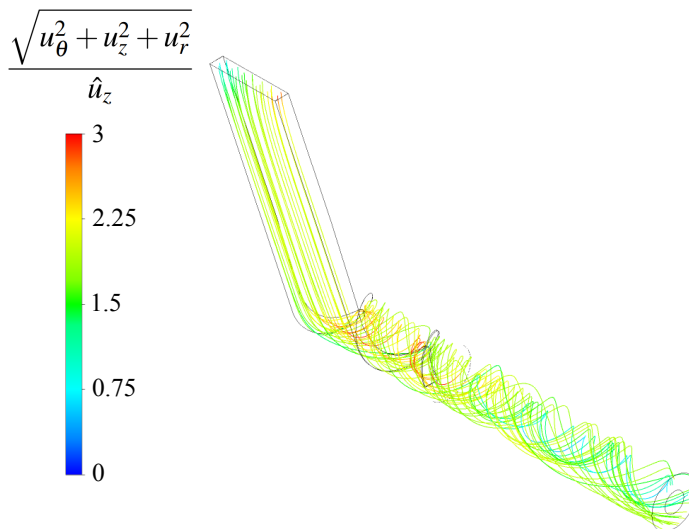
Figure 2.3: Streamlines for the N2P25 case. The streamlines are colored by the local normalized velocity magnitude.

along the z direction and swirl about the z-axis. Along the presented streamlines the velocity magnitude is generally increased within the rifling, then drops as the momentum redistributes downstream of the trailing edge. In addition, once the flow exits the rifling, the pitch of the streamlines begins to increase as the circumferential velocity begins to decay. By the exit of the domain there still exists a notable swirl component, however.

The flow development is more clearly elucidated in Fig. 2.4, which presents contours of the axial and circumferential velocity components, as well as the pressure, at various z-planes throughout the domain. Considering first the axial velocity (Fig. 2.4a), in the vicinity of the injector inlet ($z/D = -1.5$) there exists a region of relatively high velocity near the inner cylinder due to the incoming inlet flow, as well as a region of low velocity below in the injector plate. The injector plate is indicated by the white radial bar in the relevant cross-sections. The low velocity below the rifling is on the downstream side of the inclined plate, which is twisting in the counter-clockwise direction in this view as z increases (looking down the $-z$-axis). Progressing downstream to $z/D = -1.0$ and -0.5 we see that the region of low velocity on the downstream side of the plate persists. The relatively high velocity region observed at $z/D = -1.5$ is no longer apparent, being replaced instead by a region of low velocity near the inner cylinder, particularly downstream of the injector plate.
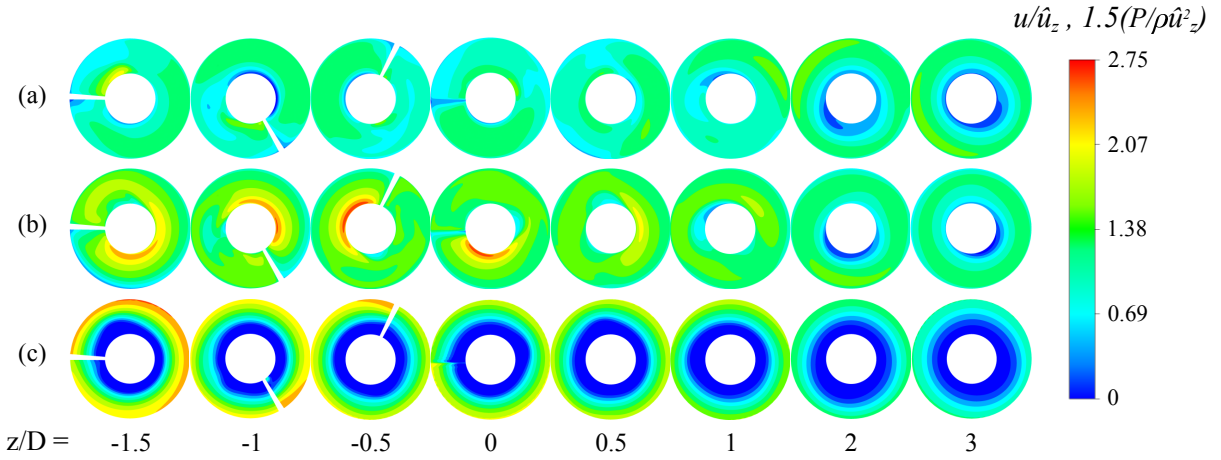
Figure 2.4: Contours showing the development of the (a) axial, (b) circumferential velocity components and (c) pressure for the N2P25 case. Velocity contours are normalized by the bulk velocity, while pressure is normalized by the dynamic pressure. The pressure is scaled by a factor of 1.5 for clarity.

At the end of the rifling, $z/D = 0$, a wake from the injector plate is observed in the axial velocity. The remainder of the cross-section is relatively uniform with regards to velocity, however. The axial velocity uniformity begins to decay by $z/D = 1$, with significantly reduced velocities near the inner cylinder by $z/D = 2$.

The circumferential velocity development is presented in Fig. 2.4b. Within the injector there is a region of high velocity on the downstream side of the plate, particularly near the inner cylinder, indicating this is the region where the rifling is primarily generating circumferential momentum. To corroborate this observation, we note that these regions of high circumferential velocity correlate well with the low axial velocity regions from Fig. 2.4a. Within one diameter of the end of the injector plate the circumferential velocity becomes relatively uniform, though some regions of higher and lower velocity are still present. Further downstream, the circumferential velocity is much lower near the inner cylinder, as it was in the axial case. Were the model to be extended further it is expected that the circumferential component would eventually completely decay through the action of viscosity.

The pressure field within the various cross-sections is presented in Fig. 2.4c. Due to the centrifugal action of the swirl injector, there is a positive pressure gradient moving radially from the inner to the outer cylinder. The pressure gradient is highest at the start of the injector ($z/D = -1.5$) and decreases through the remainder of the domain. Within the

swirl injector, the pressure on the upstream side of the injector plate is generally higher than on the downstream side. At $z/D = 0$ there is a discontinuity in the pressure at the location of the plate. Progressing further downstream, the pressure field begins relaxing towards the uniform distribution expected in fully developed pipe flow.

While the details vary from this exemplar for other test cases, the general trends are similar. In the remaining sections we use the performance metrics discussed in §2.1.2 to highlight the differences between the various cases.

2.2.2   Axial and circumferential axisymmetry

As previously discussed, the degree of axisymmetry of the flow at the rotor plane ($z/D = 0.5$) will impact turbine performance, with higher axisymmetry leading to improved rotor efficiency. The degree of axisymmetry in the axial and circumferential velocity fields at the rotor plane, computed as discussed in §2.1.2, is presented in Fig. 2.5 for all cases indicated in Table 2.1. In this figure, the average velocity deviation from the mean velocity profile $u_{i,\mathrm{asymm}}$ is presented as a fraction of the bulk velocity, $\hat{u}_\mathrm{z}$. A zero value in this plot indicates perfect axisymmetry, that is, no dependence of the velocity on θ.

Figure 2.5: Deviation of the axial (solid lines) and circumferential (dashed lines) velocities at $z/D = 0.5$ from the average velocity profiles, computed from Eqn. 2.5, versus (a) n and (b) ψ for the various pitch angles.
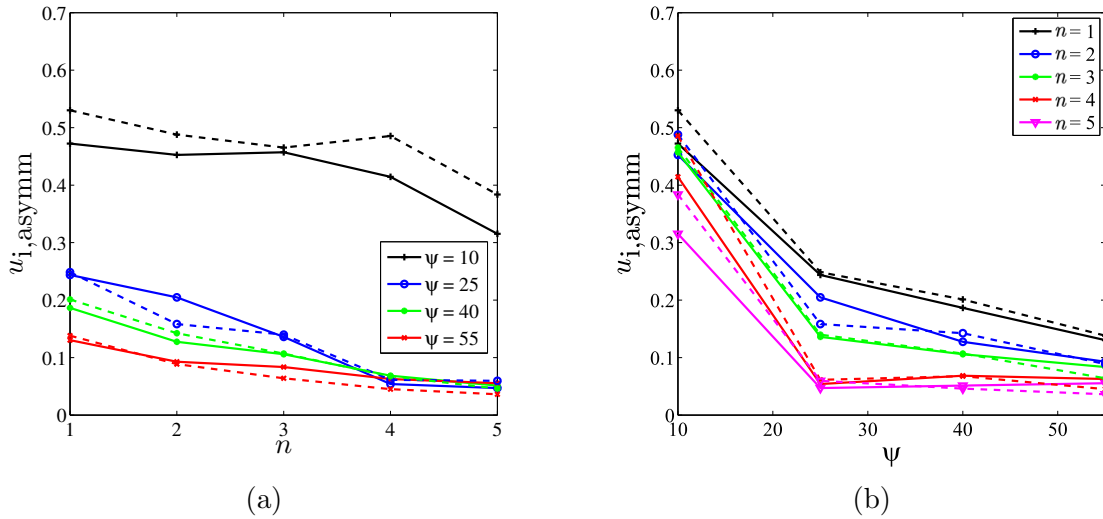
Evident from Fig. 2.5a is that the $\Psi = 10°$ case is considerably less axisymmetric, both in axial and circumferential velocities, than the other pitch angle cases. This is likely due to the steeper injection angle causing a more abrupt change in flow direction from the inlet to the rifling. Since the rotor placement plane is relative to the tip of the rifling, and since the rifling pitch is in turn dependent upon the injection angle Ψ, the larger the pitch angle, the greater the distance that the flow has available to develop before encountering the rotor (for a fixed n). Thus, for a given n, the $\Psi = 10°$ case has the shortest rifling length, and thus is the least axisymmetric. In general, the axial and circumferential velocity axisymmetry improves as Ψ increases.

Similarly, as n increases, so too does the degree of axisymmetry, indicated in Fig. 2.5b by the values decreasing towards zero. This is again a result of the flow development length. The length of the rifling section is directly proportional to the number of revolutions n, and thus increasing n provides a greater distance for the axial and circumferential momentum to redistribute and diffuse across the cross-section. The only case that does not follow this trend for all values of n is for $\Psi = 10°$, which show by far the largest degree of asymmetry in general.

2.2.3   Pressure loss and swirl number

As seen in Fig. 2.6a, the pressure loss through the device increases as n increases for all values of Ψ. There is an increase in surface area as n increases, therefore increasing the pressure loss. The trend of increasing pressure loss is especially prevalent for $\Psi = 10°$. In this case, there is a significant jump in the pressure loss between the different values of n. In the other pitch angles, there is a notable change in the pressure loss with respect to n, but it is not as severe. This difference in the n values is highlighted in Fig. 2.6b where the pressure loss is plotted against Ψ. The difference between the $\Psi = 10°$ case and the rest of the cases is once more due to sudden change in direction of the flow. This is analogous to pressure loss through pipe bends. In pipe bends, the pressure loss scales with the maximum turning angle [55]. For bends with the same radius of curvature, 90° elbows have larger pressure losses than bends of less than 90°. Applied to the rifling, the closer the inlet aligns with the x axis, the greater the losses for all other parameters fixed.

The swirl number, shown as dashed lines in Fig. 2.6a, follows a similar pattern to the pressure loss; specifically,the swirl number steadily increases with the number of revolutions, the increase is slow, with the possible exception of the $\Psi = 10°$ case. In generaly, the swirl number is largest for the $\Psi = 10°$ case and decreases steadily with increasing pitch angle. There is a relatively rapid decrease in S as Ψ increases from 10° to 25°, though the rate of change reduces thereafter.
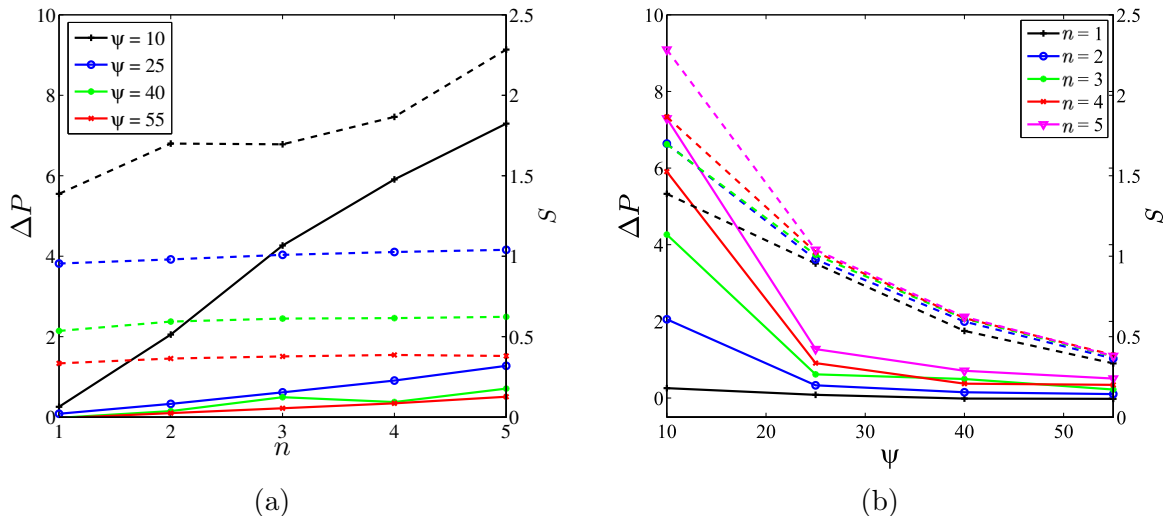
Figure 2.6: Pressure loss (solid lines) and swirl number (dashed lines) as functions of (a) n for various values of Ψ and (b) Ψ for various values of n.

Since swirl number is a measure of the amount of energy available to be extracted by the turbine, cursory inspection of Fig. 2.6a may lead one to conclude that the $\Psi = 10°$ case is the "best" design. That is, this case has the largest swirl number, suggesting that this case has the most energy available for extraction. However, the $\Psi = 10°$ case also exhibits the highest pressure losses through the geometry and has the least degree of axisymmetry of the velocity at the rotor plane, as seen in Fig. 2.5. Consequently, a more refined method must be employed in order to asses the best swirl injector design.

Another interesting feature, as seen in Fig. 2.6b, is that n doesn't have a huge influence on S. While there is an increase in S as n increases, the increase is so minimal that it can be concluded that n is not a crucial factor when it comes to the creation of swirl.

2.3 Optimization

In this section we present the results of a design optimization study for the vaneless swirl injector. As identified in §2.2, the $\Psi = 10°$ case has the highest swirl number, but also the highest pressure losses and least degree of axisymmetry. Herein we develop an objective function to condense these parameters into one measure, then perform a least squares optimization study on the objective function to deduce a set of design criteria for the

injector.

2.3.1   Objective function and optimization scheme

In order to optimize the geometry of the casing towards improving turbine performance, we formulate an objective function comprising the properties of interest, namely the swirl number, the pressure loss through the system, and the flow axisymmetry. Specifically, we wish to maximize the circumferential momentum flux, characterized by a large swirl number, minimize the pressure (energy) losses through the device, and produce a velocity field at the rotor plane with a high degree of flow axisymmetry to ensure good rotor performance over the entire casing cross-section.

To facilitate assignment of appropriate weights to the performance metrics, we normalize each metric by its maximum value in the domain. As such, each metric is bounded between zero and one. The most important property identified in the current study is the axisymmetry of the flow, which is comprised of the normalized axial and circumferential components (see Eqn. 2.5). As such, we weight the overall flow axisymmetry at 50% of the objective function, with equal weight put into both axial and circumferential symmetry. The swirl number and pressure loss are considered equally important and are weighted at 25% each. Combining these weights and metrics leads to the objective function to the minimized as

$$Q = 0.25(u_{\text{z,asymm}} + u_{\theta,\text{asymm}}) + 0.25(\Delta P) + \frac{0.25}{S} \qquad (2.10)$$

We note that the swirl number is in the denominator of its term since this metric should be maximized, while all others should be minimized.

The design optimization is performed by locating the minimum value of Q within the domain

$$\min\{Q(S, \Delta P, u_{\text{z,asymm}}, u_{\theta,\text{asymm}})\} \qquad (2.11)$$

Herein we employ a line search method to determine the minimum value of Q in the domain. Briefly, this consists of selecting a starting point in the vicinity of the minima in Fig. 2.7, determining the direction of descent using Newton's method, selecting a step size using the strong Wolfe conditions, then running a new simulation at the newly identified Ψ and n values. Values of the objective function in the vicinity of the new point are obtained through additional simulations. This procedure can be iterated until a desired tolerance or other termination criteria are met [56].

Since S, ΔP, $u_{\text{z,asymm}}$ and $u_{\theta,\text{asymm}}$ are all functions of n and Ψ, the minimization of

the objective function can be defined as:

$$\min\{Q(n, \Psi)\} \tag{2.12}$$

The optimization algorithm which is proposed for this study is the line search method. The basic idea is to select a starting point, a direction and a step size and iterate until $||\nabla Q(n, \Psi)||$ is within a certain tolerance. The optimal starting point for this particular problem is the lowest point of $Q(n, \Psi)$ since the likely-hood of the global minimum being near that point is much greater than at the other points. The iterations are defined as follows:

$$x_{k+1} = x_k + \alpha_k p_k \tag{2.13}$$

Where x_k are the initial properties of the objective function (i.e. n and Ψ), α_k is the step size and p_k is the direction.

The direction of the step taken can be decided by taking the direction of steepest descent. This direction is defined by the normalized gradient of the objective function:

$$p_k = \frac{-\nabla Q_k(n, \Psi)}{||\nabla Q_k(n, \Psi)||} \tag{2.14}$$

While this is the easiest way to determine the the direction, it is not the most effective method since it doesn't consider the curvature of the objective function. In order to take into account the curvature, a Hessian matrix is introduced into the equation (see Eqn. 2.15). This technique is commonly referred to as the Newton's method.

$$p_k = -H_k^{-1} \nabla Q_k(n, \Psi) \tag{2.15}$$

Where,

$$H_k = \nabla^2 Q_k(n, \Psi) = \begin{pmatrix} Q_{nn} & Q_{n\Psi} \\ Q_{\Psi n} & Q_{\Psi\Psi} \end{pmatrix}_k \tag{2.16}$$

Once the direction has been selected, the next step is to select a step size, α_k. The step size can be selected based on the following inequality:

$$Q(x_k + \alpha_k p_k) \leq Q(x_k) \tag{2.17}$$

However, this condition tends not to provide a sufficient decrease in Q and convergence

will be hard to achieve. In order to remedy this, sufficient decrease conditions are enforced. One set of conditions are the strong Wolfe conditions. The strong Wolfe conditions are as follows [56]:

$$Q(x_k + \alpha_k p_k) \leq Q(x_k) + c_1 \alpha_k \nabla Q_k^T p_k \tag{2.18}$$

$$|\nabla Q(x_k + \alpha_k p_k)^T p_k| \geq c_2 |\nabla Q_k^T p_k| \tag{2.19}$$

where c_1 and c_2 are constants with values of 10^{-4} and 0.9 respectively.

The step size is initially set at $\alpha_0 = 1$. This is done in order to insure that the optimal step size is within the interval of α values (i.e. $\alpha_k \in [0,1]$). If the step size doesn't satisfy the strong Wolfe conditions, then it is iterated until the conditions are satisfied [56].

2.3.2 Optimization results

The objective function constructed from the 20 test cases indicated in Table 2.1 is plotted in Fig. 2.7 as functions of Ψ and n. Evident in the contour plot is a valley in the vicinity of $\Psi = 20°$ and $n > 4$. Furthermore, the objective function is a relatively weak function of n in comparison with Ψ, suggesting that optimization efforts are better spent improving the angle than the number of revolutions. The lack of senstivity to n is advantageous, since manufacturing and installation considerations encourage smaller values of n. This reduces the overall length of the device and reduces material costs.

To begin the optimization procedure, we select $\Psi = 25°$ and $n = 4$ as the starting point, as this is cases nearest the observed minima region in Fig. 2.7. The computed descent vector is $0.45\,\hat{n} - 0.54\,\hat{\Psi}$, where the hat indicates a unit vector in the given direction. This vector indicates that Q will be reduced by increasing n by approximately half a revolution while decreasing Ψ by less than half a degree. Comparing the value of Q at $n = 4$ and $\Psi = 25°$ and the value after the first step reveals a change of less than 3%. Given the very small step in the $\hat{\Psi}$ direction, the relatively insensitivity of Q to n in Fig. 2.7, and the modest change in Q we terminate the optimization procedure after the first step. Given the desire for shorter overall devices and minimizing manufacturing expense, we recommend that this particular vaneless swirl injector design be manufactured with $n = 4$ (or less) and $\Psi = 25°$.
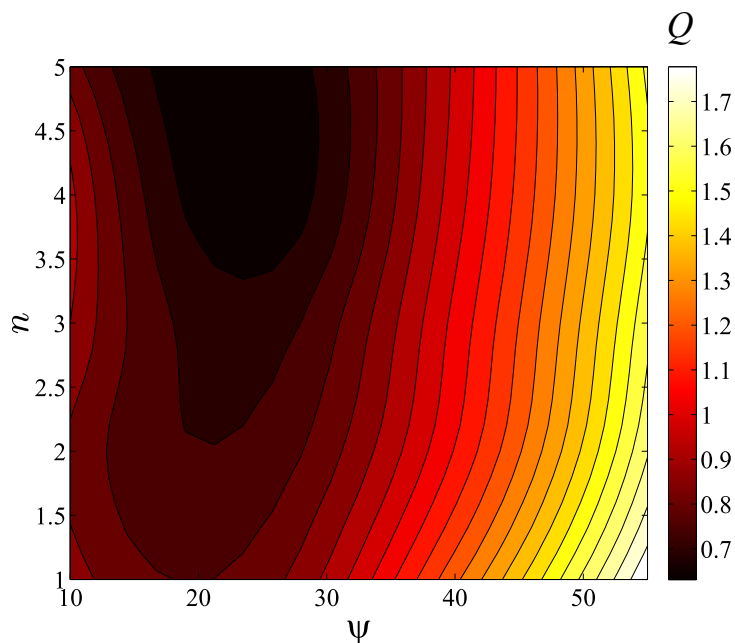
Figure 2.7: Contour plot of the objective function used for optimizing the vaneless swirl injector geometry.

2.4 Summary and conclusions

A "fish-friendly" vaneless swirl injector design developed by AlfaStar Hydro was numerically investigated to develop geometric design guidelines for efficient operation. The swirl injector is intended to replace traditional inlet guide vane arrays in water turbines, which are responsible for conditions leading to fish mortality in the field. To ensure efficient operation of a water turbine employing the vaneless swirl injector, the flow downstream of the injector should be relatively uniform in the rotor plane, have high swirl, and the pressure losses should be minimized. A series of swirl injector designs with varying pitch angles and number of revolutions of the swirl injector were considered.

In general, the velocity and pressure fields within the swirl injector became increasingly axisymmetric as the number of revolutions and the pitch angle increased. Increasing either variable increased the overall length of the injector, thus leading to a greater flow development distance, which improved flow axisymmetry. The swirl imparted to the fluid and the pressure losses through the device increased with increasing number of revolutions and decreasing pitch angle. As the number of revolutions increases, the length of the rifling increased, leading to a larger swirl component, but also increased the surface area

upon which friction could act, which increased the pressure losses. Decreasing pitch angle increased the swirl number, thus increasing the energy available for the turbine to extract, but also rapidly increased the losses through the device.

Design optimization of the swirl injector was performed by constructing an objective function from four key metrics at the rotor plane; axisymmetry of the axial flow, axisymmetry of the circumferential flow, the pressure losses from the inlet to the rotor plane, and the swirl number. The first three metrics were to be minimized, while the latter was to be maximized. The optimization study results indicated that the objective function is much more sensitive to the pitch angle of the swirl injector than to its number of revolutions. A pitch angle of 25° with 4 revolutions was found to be optimal. In practice, however, overall device length is a concern. Given the relative insensitivity of the device performance on the number of revolutions, it is recommended that the pitch angle be set and overall device length be controlled via the number of revolutions.

Chapter 3

Development of a swirl injector test rig with an attached nose cone

The experimental setup was designed with the intention of testing the pressure and velocity characteristics of the swirl injector and validating the numerical simulations. The overall design of the experimental facility, as well as the specific design and selection of each of the components in the setup, will be discussed in this chapter. The assembly of the system will also be discussed.

3.1 Design

The main components of the experimental setup are the reservoir, the pump, the gate valve, the circular-to-rectangular transition, the flow conditioning elements, the swirl injector, the test section, and the flow meter. The whole system, which is shown in Fig. (3.1), is a recirculating setup. Starting from the reservoir, the fluid flows into the intake of the pump. The flow continues through to a T-section, in which one branch goes to the rest of the experimental setup, and the other branch goes back to the reservoir. The branch going back to the reservoir has a ball valve for rough flow control. The branch going to experimental setup has a gate valve attached in order to be able to perform fine flow control. This bleed system allows for better control of the flow through the setup.

The flow going to the rest of the experimental setup goes through a transition section, which was designed to transition from a circular to rectangular cross-section. After the transition, the flow enters the flow conditioning elements, after which the flow enters the
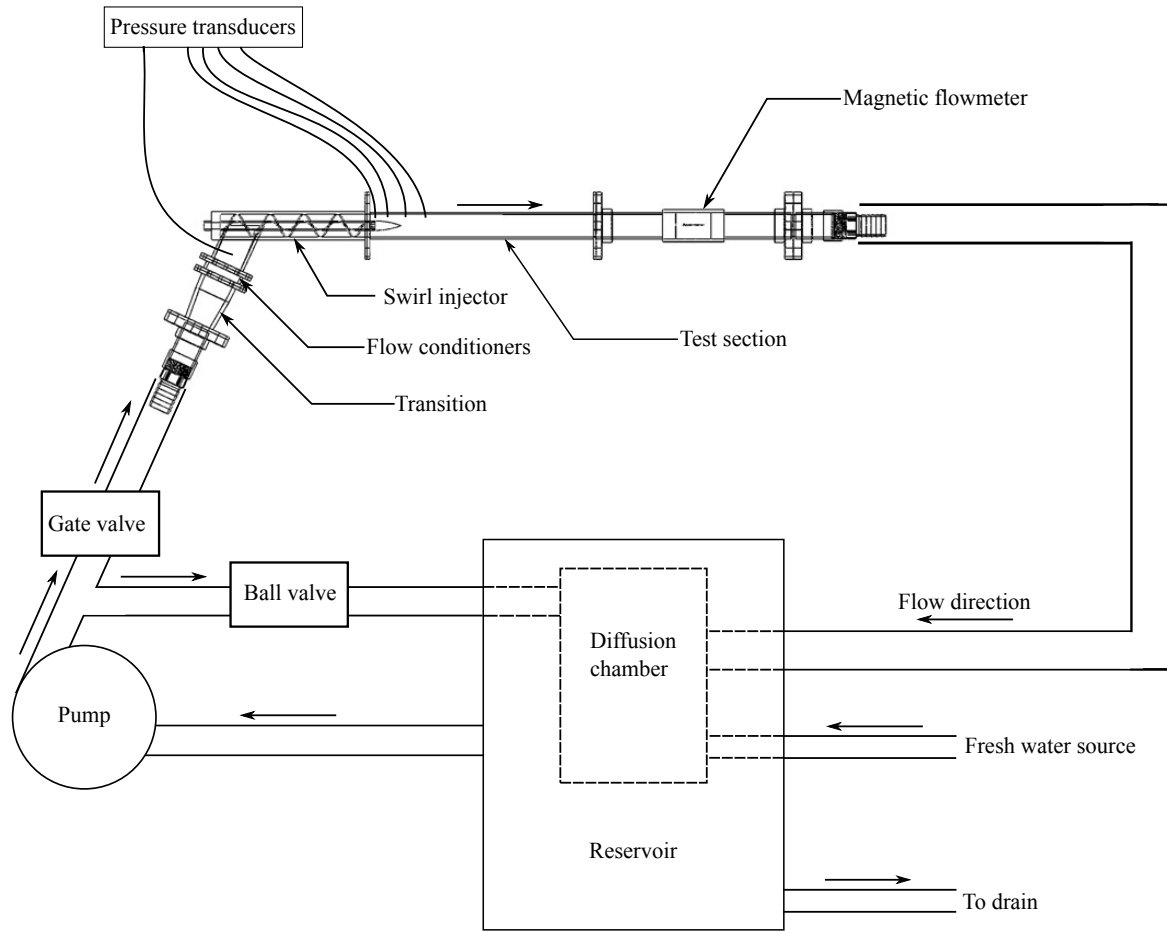
Figure 3.1: Experimental setup diagram.

swirl injector itself. After the swirl injector, the flow passes through to the test section. The flow then proceeds through the magnetic flow meter, which reads out the bulk flow rate. After the flowmeter, the flow returns to the reservoir to be recirculated through the system.

3.1.1 Swirl injector

Based on the results of the numerical investigation, the swirl injector design selected for experimental validation has 4 revolutions and a pitch angle of 25°. As seen in Fig. 3.2, the injector is made up of seven distinct parts: 2 half-tubes which make up the body, an auger with an inlet, a transparent inlet box, a back plate, and 2 flanges at the inlet and the outlet.

A rectangular channel forms the entrance of the swirl injector. The box is made of acrylic in order to allow optical access to the flow entering the injector. There is also a flange attached to the acrylic box in order to be able to attach the injector to the circular-to-rectangular transition and any flow conditioning elements. There are also 4 pressure taps on the acrylic box, one on each of the sides of the box. The taps are 3 mm from the border between the ABS inlet and the acrylic and at the center of the box.

The auger and inlet were 3D printed in order to simplify the construction process. The University of Waterloo's 3D Print Center manufactured the part using the Stratasys Dimension 1200es 3D printer. The printer can function on a layer thickness of either 0.33 or 0.127 mm for ABS. The finer resolution (0.127 mm) was used in order to make sure that the part would have minimum roughness. Another advantage of 3D printing the auger/inlet assembly is the added sturdiness of having the whole assembly constructed
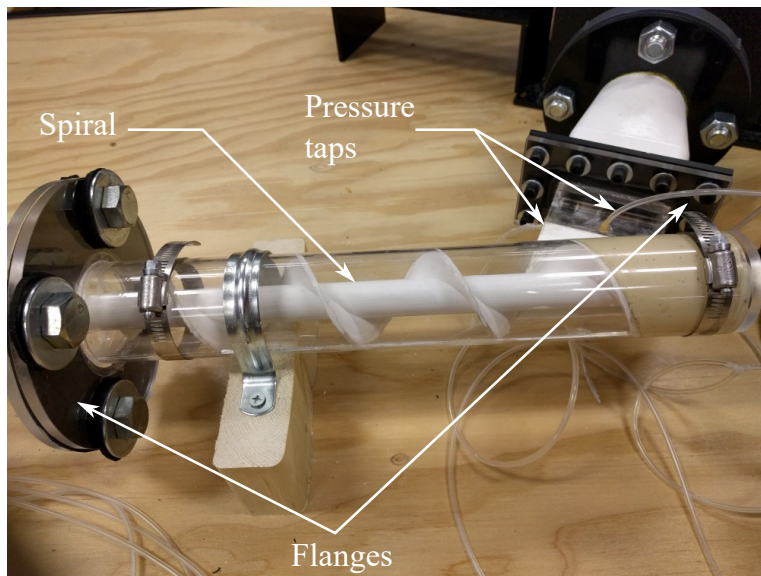
Figure 3.2: Swirl injector as installed in the experimental setup.

Figure 3.3: The swirl injector with the unused section filled in with the epoxy-filler mixture.

from one piece. The main reason for selecting ABS is due to the strength of the bond between ABS and acrylic when fused together using acrylic cement (SCIGRIP 16 10315 Acrylic Cement, Clear). The acrylic cement acts much like the ABS cement, wherein it melts the surface layer of the ABS, which allows for a stronger bond between the ABS and the acrylic once the compound has dried. The ABS part was sanded in order to remove any roughness on the surface, and a clear coat of paint was applied onto the part in order to water-proof it, since the 3D printing process causes there to be micro holes in the part.

The shell of the injector is made up of two halves of a 0.0508 m acrylic pipe. The acrylic halves were glued to the 3D printed auger with acrylic cement. The seams where the two halves meet was sealed using an epoxy compound. In order to ensure that the two halves remained intact, two hose clamps were added to the model: one at the outlet near the circular flange and one at the rear.

The portion of the injector which does not see flow going through it was filled in with an epoxy-filler mixture, as seen in Fig. 3.3. This was done to ensure that water would not leak out of the back of the injector. Once the mixture settled and dried, the backplate was added to the rear. The backplate adds an additional level of leak proofing, though the epoxy-filler mixture alone is likely sufficient for sealing.

Figure 3.4: The swirl injector with nose cone.

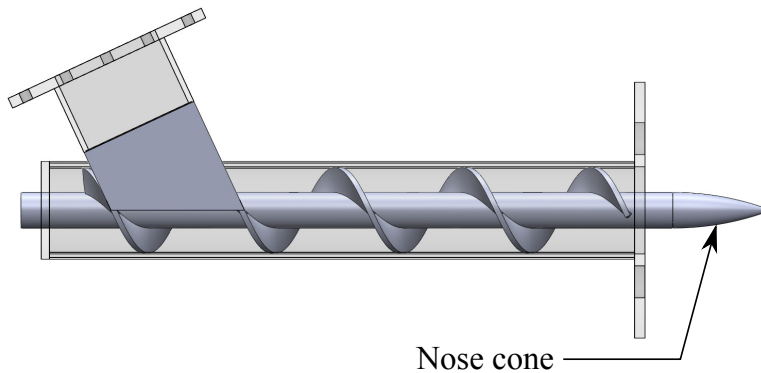The tip of the injector has an ogive-shaped nose cone attached to it, as seen in Fig. 3.4. The nose cone reduces the effects of flow separation and the resulting negative effects that has on the flow, such as large recirculation regions which create additional turbulence. The nose cone was also 3D printed with ABS. There is a threaded center hole which is attached to a threaded rod which is used to hold the nose cone in place. It should be noted that the nose cone was added after the optimization was done and therefore is omitted in the optimization study. The nose cone was omitted for simplicity.

3.1.2 Reservoir

The reservoir is composed of two vessels, as seen in Fig. 3.5. The larger vessel can contain up to 400 gallons of water, while the smaller vessel can hold roughly 250 gallons. The main reason for adopting this two-vessel model for the reservoir is to mitigate the entrainment of air bubbles in the intake pipe for the pump and the accumulation of air bubbles in the test section. The flow from the system enters the reservoir at a high velocity, the high velocity jet had the tendency to entrain air bubble from the free surface down into the reservoir. These air bubbles would end up being sucked up by the intake for the pump, and accumulating in the test section (see Fig. 3.6). The accumulation of bubbles hindered velocity measurements and reduced pump efficiency if a significant amount of air was entrained.

The solution adopted herein is to have the intake in a separate reservoir than the outflow. The outflow goes into the smaller vessel, wherein the air bubbles are separated from the intake. The water overflows from the smaller vessel into the larger reservoir. The intake is located at the bottom of the larger reservoir, such that any air bubbles originating
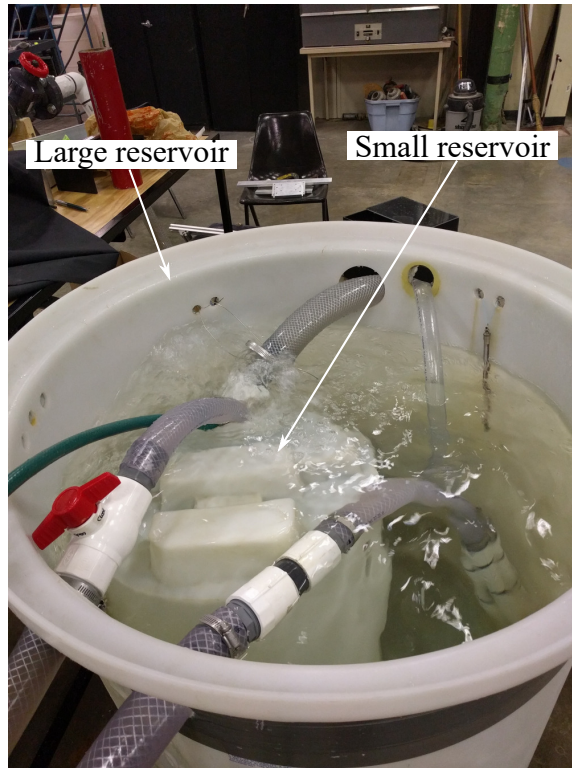
Figure 3.5: Reservoir used for the experimental setup.

from the outflow would not be able to enter the intake.

The recirculation of the water through the system increases the temperature of the water in the reservoir. The increase in temperature has an influence on the viscosity of the water, and therefore can change the Reynolds number, and thus the flow characteristics. Furthermore, a stable temperature is needed in order to minimize any uncertainty in the measured values. In order to mitigate the influence of the temperature, a siphon-based heat exchanger system was implemented. A fresh water source is brought in to the small vessel and a outflow tube is placed in the larger vessel. The outflow leads to a drain located beneath the system. This constant refreshing of the water ensures that the temperature stays at a steady 21 ± 0.5 °C.
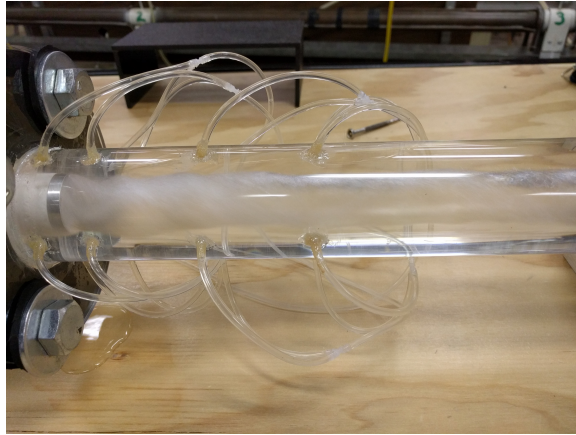
Figure 3.6: Accumulated bubbles in the middle of the test section.

3.1.3 Pump

The sizing of the pump was done by estimating the required pressure and flow rates by using the one-dimensional energy equation with pressure loss. The estimations were then used to properly size the pump and the flow meter used in the setup. The initial sizing for the pump was done considering the losses through six 90° bends, a set of honeycombs and a gate valve. The pump was sized in order to function within the lower operational range of the turbine (2 to 5 meters of head).

The selected pump is a 2 HP open drip proof AMT self-priming centrifugal pump, seen in Fig. 3.7a. The maximum output of the pump is 102 GPM (6.4 l/s) at 30 ft (9.1 m) of head (as seen in Fig. 3.7b). The motor is a single phase motor which is controlled by a simple on-off switch. The inlet and outlet of the pump are 1.5 inch female NPT threaded. The self-priming feature was necessary due to the nature of the line coming from the reservoir. The intake line comes from the top of the reservoir, and therefore is largely empty. This would choke a standard pump, but the self-priming pump is able create suction through its priming cycle. The pump is attached to the table via a mounting plate which is welded to the frame of the table.

3.1.4 Circular-to-rectangular transition

The transition is a necessary part of the setup since the inlet for the injector has a rectangular cross-section, whereas the pipe has a circular cross-section. The transition was designed
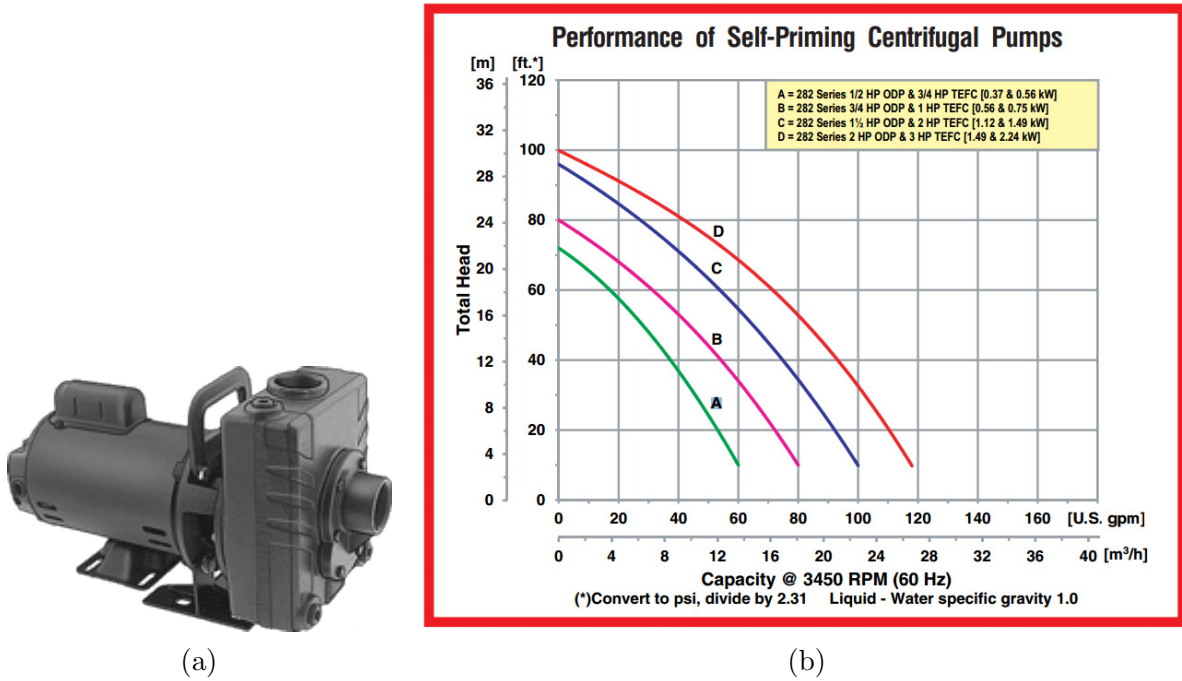
Figure 3.7: Illustration of the pump (a) used in the experimental setup as well as the total head versus flow rate curve (b) for the pump provided by the manufacturer. Curve "D" is used for the pump used in the experiments [57].

according to a study by Atilgan et al., in which they discuss the a design paradigm for making circle-to-rectangle and rectangle-to-rectangle transitions [58]. The study elucidates the relationship between the required length between the two cross-sections and the equivalent cone half-angle. The optimal cone half-angle in order to minimize head loss is 5° [59]. Using this criteria, the length of the transition is determined. A primary assumption of the paradigm is that the area of both cross-sections are equivalent. In the present case, the actual area of the inlet to the injector is smaller than the circular cross-sectional area. Therefore, there is a nozzle section on the transition in order to match the inlet cross-section of the injector.

The main body of the transition was 3D printed out of ABS (as seen in Fig. 3.8). The 3D printed part was sanded down and given a clear coat of paint in order to water-proof it. There are ABS flanges that were glued onto the transition using ABS cement. The ABS cement melts the surface of both parts, which makes the transition and flanges into one piece.
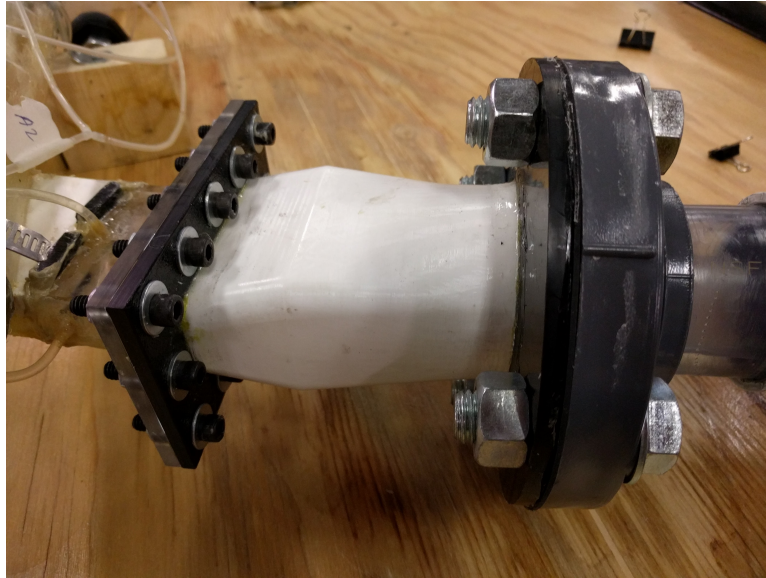
Figure 3.8: Circular-to-rectangular transition (in white) with flanges (in black).

3.1.5 Flow conditioners

The flow entering the injector has a high degree of turbulence (approximately 20% based on inlet velocity measurements) since the flow is coming directly from the pump. To reduce the turbulence intensity, a flow conditioner is inserted upstream of the swirl injector. The flow conditioning used for the setup consists of a screen attached to an array of honeycomb. Honeycomb is used in flows in order to reduce the lateral component of the turbulence. This component is essentially eliminated within a length of 5-10 cells widths. Furthermore at the exit of the honeycombs, the flow is almost perfectly axial. For the full benefits of the structure, the length to diameter ratio should be 6 to 8 [60]. Screens are mainly used to make the flow uniform in the axial direction by producing a static pressure drop and reducing the boundary layer thickness. The optimal open area ratio is greater than 57%. Below this there are instabilities in the flow. Usually a series of screens are used in order to produce a uniform and gradual pressure drop. In order to achieve pressure drop independence the screens need to be placed at a certain distance away from each other [60]. The limit is about 500 wire diameter apart, past which there is no change in effectiveness [61].

The key characteristic in defining the performance of a flow straightener is the pressure-loss coefficient (K), which is defined as [62, 63]:

$$K = \frac{\Delta P}{\frac{1}{2}\rho U^2} \tag{3.1}$$

where ΔP is the pressure gradient across the straightener, U is the average downstream velocity, and ρ is the density. For screens, at $K = 2$, most axial fluctuations are removed [60]. Another formulation of K for screens, proposed by Wieghardt, is [62]:

$$K = 6.5 \left(\frac{1 - \beta}{\beta^2} \right) Re_d^{-1/3} \tag{3.2}$$

where $Re_d = Ud/\beta\nu$ is the Reynolds number through the straightener, d is the wire diameter, β is the open area ratio and ν is the kinematic viscosity of the fluid. The latter formulation is more useful since the pressure loss coefficient can be obtained using the geometry of the screen. The open area ratio for screens is defined as follows:

$$\beta = \frac{(M - d)^2}{M^2} \tag{3.3}$$

where M is the mesh length and d is the diameter of the wire (see Fig. 3.10).

The screen used in the setup has a β-value of 70% ($d = 0.11$ mm, $M = 0.67$ mm) which is well over the required value. The pressure loss coefficient for the screen is calculated to be $K = 3.75$ at the operational bulk velocity of 2.6 m/s. The bulk velocity was calculated by using the volumetric flow rate (151.42 l/min) and the area of the rectangular inlet.

The honeycomb, as seen in Fig. 3.9, has a cell diameter of 1.5 mm and a cell length of 13 mm. The length-to-diameter ratio is therefore is 8.67 which is in the acceptable range. The pressure loss coefficient for the honeycomb was calculated to be 0.26. The K-value was obtained for the same flow rate as the screen.

3.1.6 Test section

The test section consists of a 0.508 m long acrylic tube with an inner diameter of 0.0508 m and a wall thickness of 0.003175 m. Acrylic was chosen in order to have optical clarity to
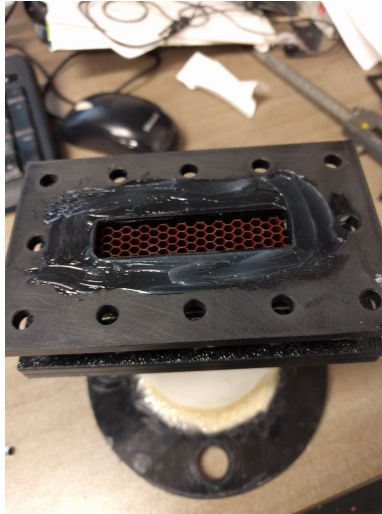
Figure 3.9: Honeycomb array attached to the transition.
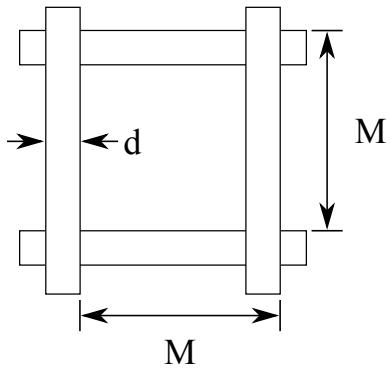
Figure 3.10: Dimensions used to calculate β

enable the use of laser Doppler velocimetry (LDV) and other optical techniques in order to characterize the flow velocity. There are pressure taps drilled into the test section at the D0.5, D1, D2 and D3 cross-sections. There are 4 evenly spaced pressure taps around the circumference of the tube (see Fig. 3.11). There are two flanges on either side of the tube such that the test section can be attached to the injector and the downstream elements.
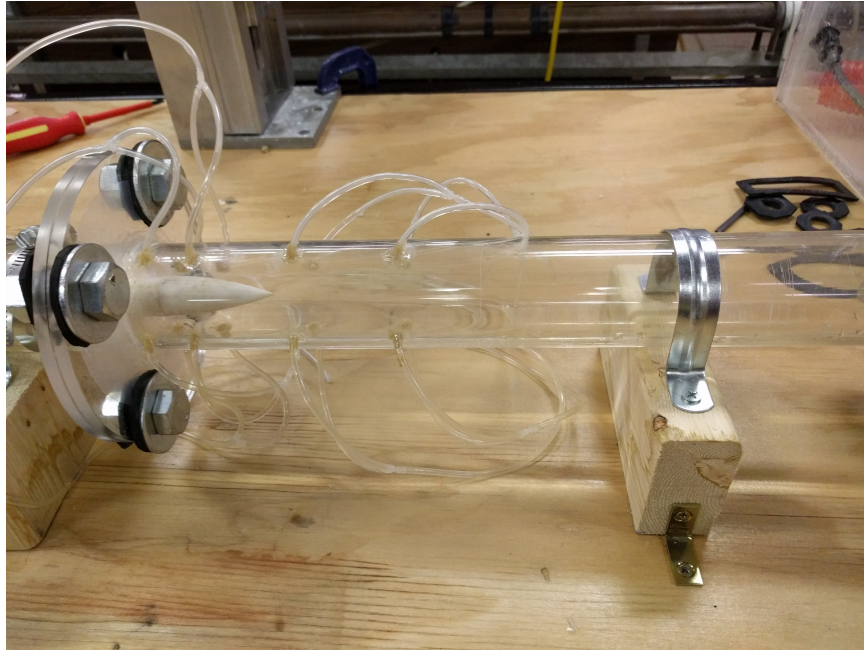
Figure 3.11: Test section with pressure taps. The nose cone attached to the injector can also be seen in this figure.

3.1.7 Pressure sensors

The pressure taps are made up of flexible 0.003175 m inner diameter tube which were glued into the holes made for the taps. The tap holes are 0.003175 m in diameter and are drilled perpendicularly to the tube. The tubes are inserted in to the holes, ensuring that the tubes are perpendicular to the wall. The tubes sit flush with the inner wall of the test section, which was verified manually by a visual and tactile inspection. The tubes were glued using a plastic epoxy. The tubes from the 4 taps (at each of the cross-sections and at the inlet) can be combined into one tube connected to a pressure sensor, thus giving the average pressure at the cross-section, or individually attached to difference pressures to obtain more spacial information. In standard operation, there are 5 pressure sensors, one for each of the cross-sections and one for the inlet.

Honeywell ABPDANT005PGAA5 pressure sensors are used for recording the static wall pressures. They are gauge pressure sensors with a gel coating on the inner membrane, in order to prevent damage from moisture. They are designed to measure between 0 to 5 psig (0 - 34473.8 Pa) with a voltage range from 0.5 to 4.5 V. The accuracy of the sensor is $\pm$ 0.25% of full scale. The sensors have a 0.002032 m diameter barbed tip that attaches the
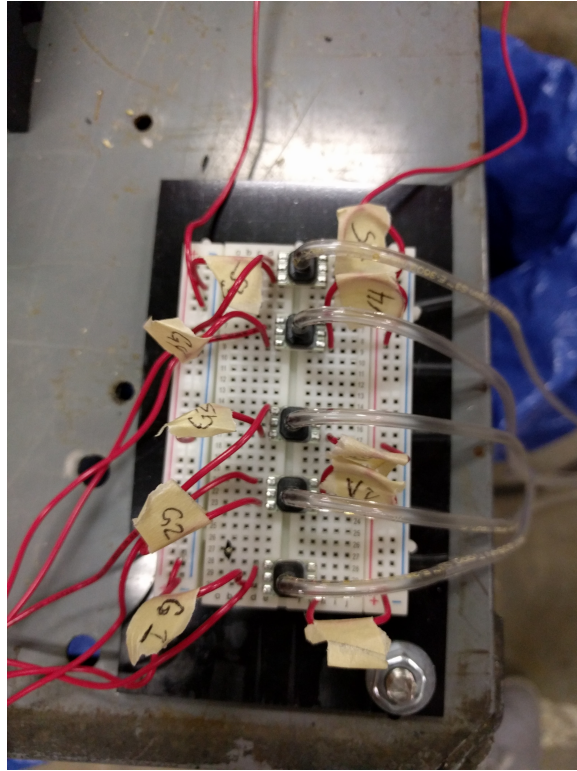
Figure 3.12: Breadboard containing the pressure sensors.

sensors to the tubing.

A breadboard is used to connect all of the sensors (as seen in Fig. 3.12) to a National Instruments NI SCB-68 Data Acquisition module connected to a National Instruments PCIe 6323 DAQ card. The sensor array is powered by a variable power source, which was set to 5 V. A LabView VI was created in order to collect the data from the transducers. The VI collects the voltage output from the transducers and writes the data points on an Excel sheet for data analysis.

The sensors were calibrated using a custom hydrostatic calibration setup consisting of a hose attached to a base. The base contained 5 taps on the bottom which were attached to the pressure transducers. The base and the hose were filled up with water. The calibration was done by lifting the hose to different heights and collecting the voltage output for 10 seconds. The average voltage output was then calculated for each of the sensors at the various heights. This process was done for 20 evenly-spaced points along the operational range (between 0 and 3 meters of head). The voltage data were collected 2 times from 0

to 3 meters and 2 times from 3 to 0 meters. A linear fit was then applied to each of the sensor data sets. The average error on the fits was less than 2%. The data sets, along with their linear fits, can be found in Figures 3.13a to 3.13e.
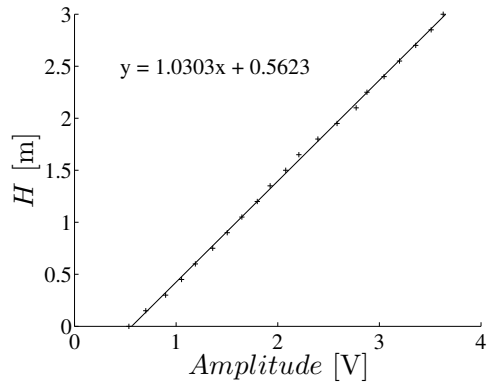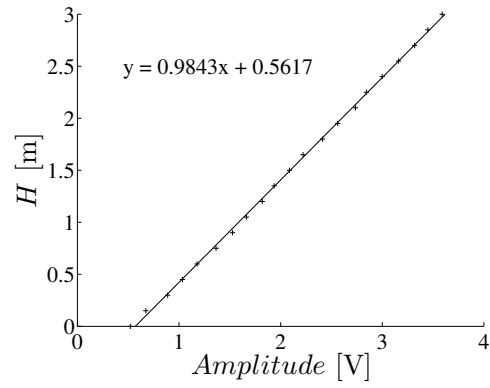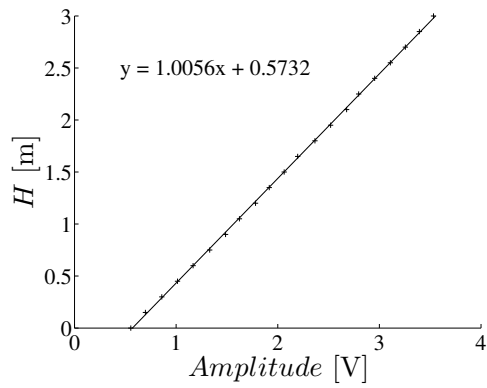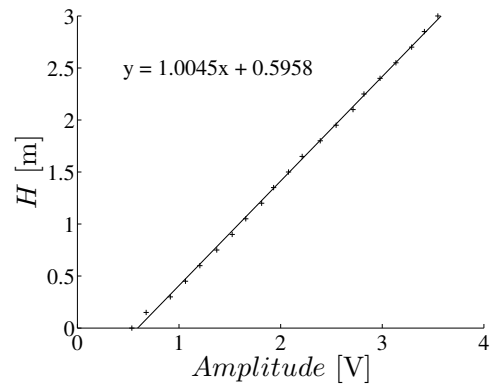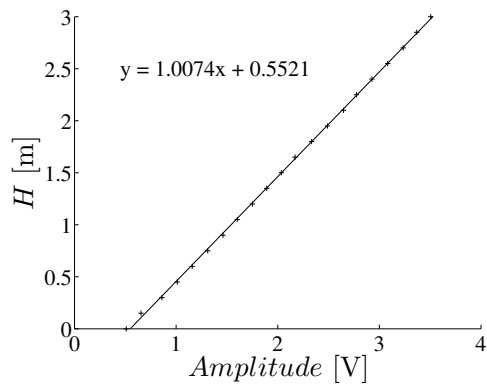
Figure 3.13: Calibration curves with linear fits for the (a) inlet, (b) D0.5, (c) D1, (d) D2, (e) D3 pressure transducers.

3.1.8   Flow meter

A selection of flow meters were explored for the setup. Initially, an orifice plate meter was proposed in order to measure the flow rate through the system. This solution was rejected due to the errors caused by the swirling flow upstream of the flow meter, as well as the possibility of cavitation due to the high pressure loss across the plate [64, 65].

The final solution was to implement a magnetic flow meter as seen in Fig. 3.14. The Omega FMG802 battery operated magnetic flow meter was selected for the setup. The main reason for selecting a magnetic flow meter is for the low upstream and downstream straight pipe requirements. In other words, the selected magnetic flow meter only required 5 diameters of straight pipe upstream and 1 diameter downstream. The meter has an error of 1% on the reading and is able to measure flow rate between 6 to 300 GPM.
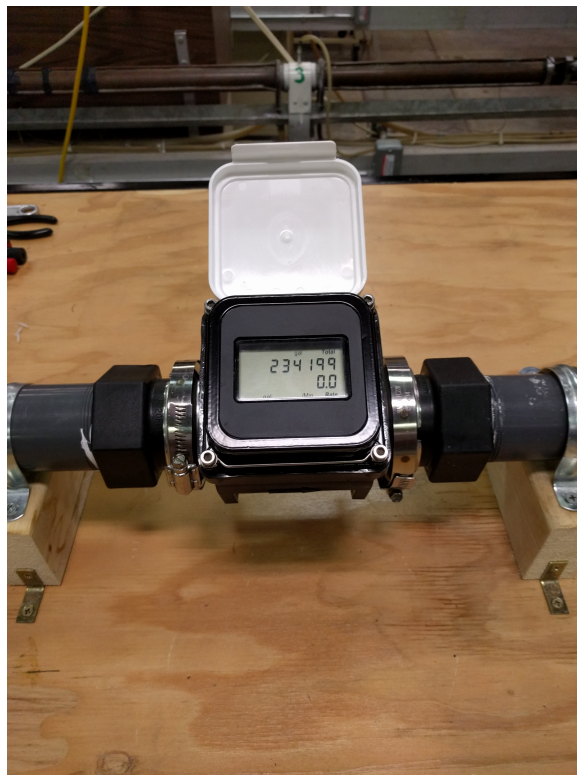
Figure 3.14: Flow meter as installed on the setup.

3.1.9 Table

The entire setup, with the exception of the reservoir, is mounted on a 2.25 m by 1.25 m table. The frame for the table was custom welded in order to be able to hold upto 200 lbs. The frame is made up of 0.0254 m square hollow steel rods. There is also a platform for installing the pump. The top of the table is made of plywood so that the supports needed for the piping could be drilled in directly without much effort. A clear coat of paint was applied to the top of the plywood in order to waterproof it.

All of the parts of the setup are either made up of ABS or PVC. Therefore either ABS or PVC cement was used to assemble the individual components. Each of the assemblies were then attached to each other by flanges. Between the flanges was usually a gasket in order to prevent leaking. In the case of the flanges on the injector, silicon was used in order to leak proof the connection.

3.2 Measurement techniques

The two major measurement techniques which are used to characterize the flow through the swirl injector are Laser Doppler Velocimetry (LDV) for the velocity measurements, and pressure sensors for the pressure measurements. A thermometer was also used in the reservoir in order to monitor the temperature level and a magnetic flow meter was used in order to monitor the bulk velocity going through the system. The following section will delve into the details of these measurement techniques and tools.

3.2.1 LDV measurements

The LDV system is a Measurement Science Enterprise miniLDV system. It is a single component measuring LDV system with a standoff distance of 400 mm and a fringe separation is 4.170 μm [66]. The table used to mount the experimental setup was sized with respect to the standoff distance. The probe is mounted on to a 2-axis manual traverse. The beam deflection is compensated by using the beam deflection compensation method as described in Appendix A.

The traverse allows the probe to be positioned in the x and y directions as defined by Fig. 3.15. The horizontal points are measured along the x-axis (at y = 0). Five evenly spaced points are measured per side, therefore 10 points are measured along the x-axis.

The velocities are measured at the D0.5, D1, D2 and D3 planes. Due to the obstruction caused by the pressure taps, the actual measurement is taken at 5 mm downstream of the plane for the D0.5, D1, D2 and D3 planes (see Fig. 3.16). Therefore the actual planes are D0.598, D1.098, D2.098 and D3.098. For simplicity's sake, for the velocity measurements, these planes will be referred to as the D0.5, D1, D2, D3 planes. It should be noted that for the pressure measurements, the D0.5, D1, D2 and D3 locations are based on the physical positions since the pressure taps were positioned there.

The two components of velocity which are measured are the axial and circumferential velocities. The axial velocity component is measured by aligning the LDV horizontally with respect to the test section. In order to measure the circumferential velocity component, the LDV laser beams are positioned vertically. A leveled plate with a crosshair is used to align the laser beams.
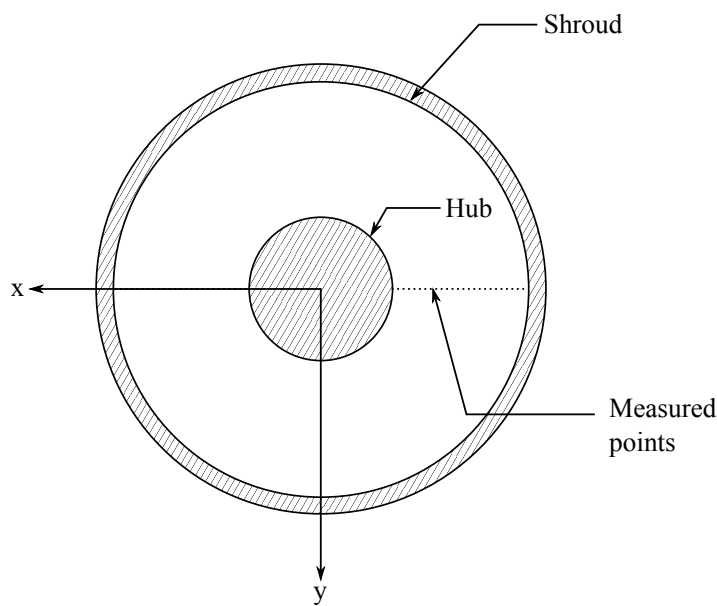

Figure 3.15: Locations of the measured points. The coordinate system used is also displayed.
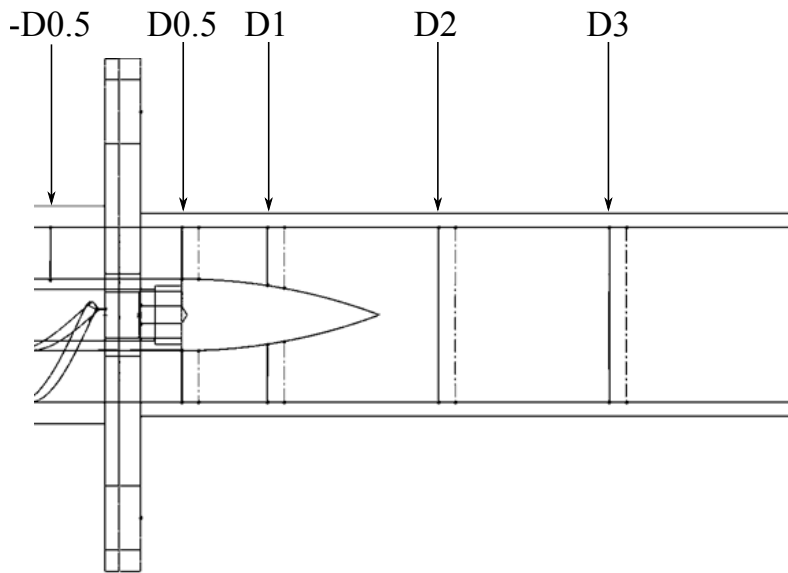
Figure 3.16: Theoretical locations (solid lines) and actual locations (dotted lines) where the measurements were taken.

3.2.2 LDV uncertainty and data processing

The main source of uncertainty in LDV measurements is due to velocity bias. Velocity bias error is typically caused by the tendency of the LDV probe to detect higher velocity particles as they travel through the probe volume [67, 68]. The uncertainty error is described as the discrepancy between the true velocity value, $u_{i,T}$, and the measured velocity, u_i where the index i is either z or θ depending on the velocity component being investigated. The true velocity can be approximated by solving Eq. 3.4 which provides the relationship between the true velocity, the measured velocity and the RMS fluctuation in the measured velocity $(\bar{u}'_i)$:

$$\frac{u_i}{u_{i,T}} \approx 1 + \frac{\bar{u}'^2_i}{u^2_{i,T}} \tag{3.4}$$

After obtaining the true velocity, the percent difference between the true and measured values is subsequently used as the uncertainty on the measured value. The uncertainty on the measurement can be reduced by re-sampling the data to a constant frequency. The velocities are typically measured at different frequencies, and by re-sampling the velocities at the same frequency, the error can be reduced [67]. The raw velocity data is also filtered by excluding any data points which are 3 standard deviations away from the mean. Since 99.7% of the data is found within 3 standard deviations, the neglected points are considered outliers and therefore unnecessarily skew the results [69]. The LDV probe itself has an overall accuracy of 0.3% on the measured value which is considered negligible when compared to the velocity bias error [66]. The probe was aligned using a digital level with a $\pm 0.1°$ resolution and the traverse used to displace the probe has an uncertainty of $\pm 0.13mm$ both of which are considered negligible when compared to the bias error.

3.2.3 Pressure measurements

The sensors described in Section 3.1.7 are used to measure the axial pressure distribution. The pressure is measured at the 4 pressure taps evenly placed at the D0.5, D1, D2, D3 cross-sections and at the inlet cross-section. As described in Section 3.1.7, the measured locations are the physical locations on the tube. The pressure detected by the sensor is the average pressure at the cross-section. The data is collected simultaneously for all the locations for 10 seconds at a 1000 Hz. The pressure which is measured is the gauge pressure.

The sensor heads can be reconnected in order to measure individual pressures circumferentially at a specific cross-section, as opposed to measuring the average pressure at each cross-section. This reconfiguration is done to verify the uniformity of the pressure at the cross-section.

3.3   Characterization results

The following section will discuss the charaterization results of the experimental setup. The characterization of the setup was done by measuring the velocity drift in the test section, the temperature fluctuations in the reservoir, and the inlet velocity profile.

3.3.1   Velocity drift
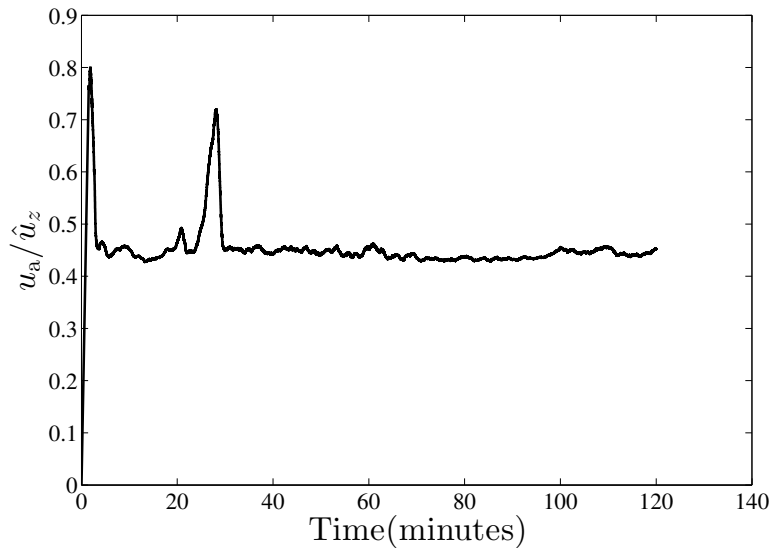
Figure 3.17: Rolling average of the normalized measured velocity versus time in minutes.

In order to begin collecting data from the experimental setup, the settling time for the system was needed. In order to determine this, velocity data was measured using the LDV at the D3 cross-section. The axial velocity component at r/r_o = -0.33, was measured for 2 hrs. Once the data was collected, the rolling average was calculated with a window of 15000 samples (as seen in Fig. 3.17). The percent difference was calculated between the
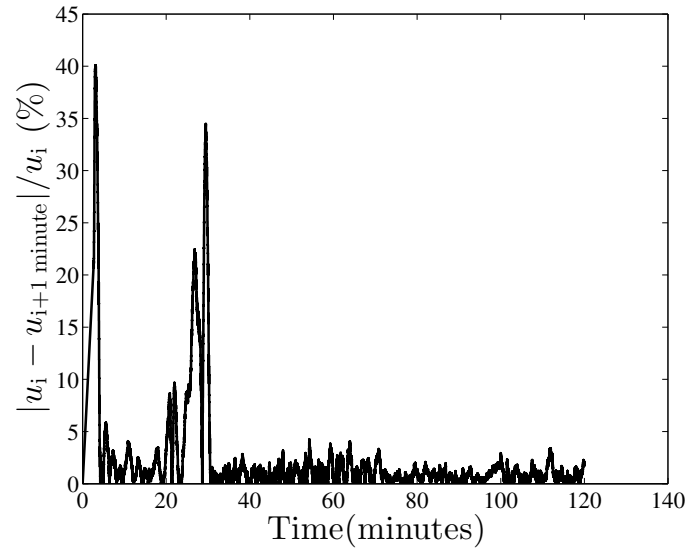
Figure 3.18: Percent change in the rolling average versus time in minutes.

rolling average values with respect with time. Due to the data rate (about 300 samples per second), the rolling average didn't change much from point to neighbouring points. Therefore, the percent difference was taken between points which were 1 minute apart, yielding a much more significant result since the percent difference between the points was amplified, as seen in Fig. 3.18.
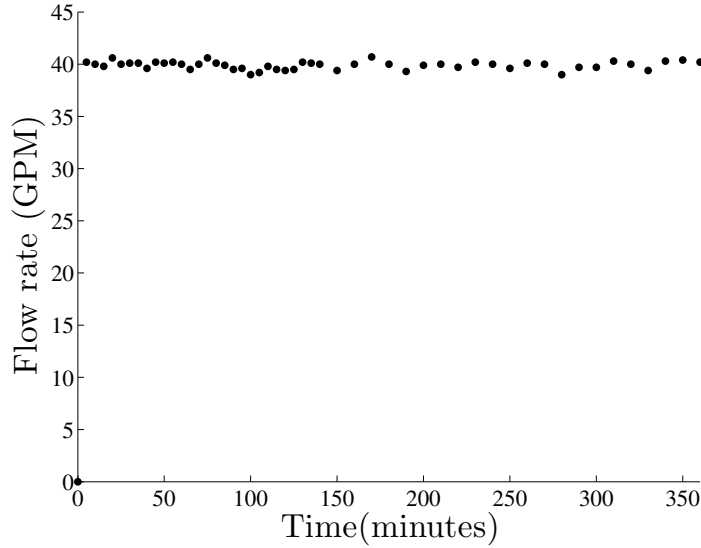
Figure 3.19: Flowmeter readings over the measurement time.

As seen in Fig. 3.17, the system settles after 40 minutes. The average percent difference after 40 minutes is 0.88%. Past the 40 minute mark there are no random peaks in the velocity. Before the forty minute mark, random peaks have been observed at 15 and 20 minutes for multiple runs. It is unknown exactly what caused these spikes, but they are present at the same times in all the replicated runs. The flow meter readings (seen in Fig. 3.19) show a standard deviation of 0.38 GPM (0.024 l/s), or 0.95% of the operational flow rate of 40 GPM (2.5 l/s) for the measured period. The readings for the flow meter were taken for every 5 for the first 140 minutes and 10 minutes until the end of the LDV run. No major spikes are seen during the measured time, but due to the spikes seen in LDV readings the data collection will be started after the 40 minute mark.

3.3.2 Temperature

The temperature is monitored in the reservoir. A constant temperature is required in order to avoid any variation in the viscosity of the working fluid. In order to quantify the change in temperature, it was recorded for 70 minutes without the syphon system. After the 70 minutes, the syphon system was engaged and the temperature was monitored for an additional 70 minutes. The temperature was recorded every 5 minutes during the first 140 minutes and every 10 minutes until the end of the experimental run.

54
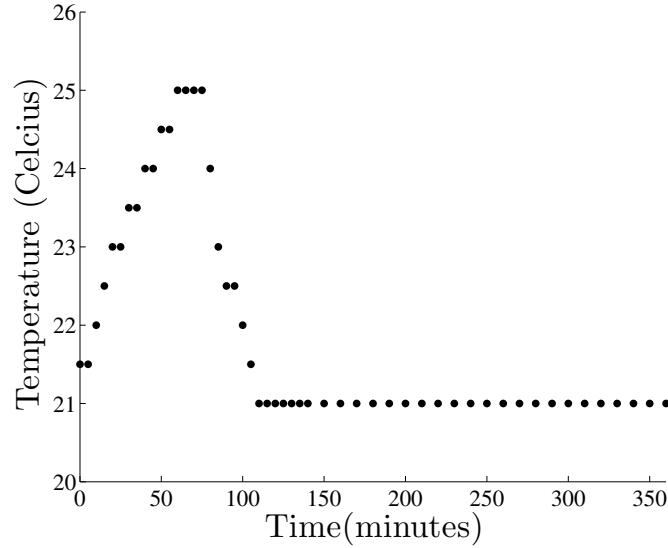
Figure 3.20: Change in temperature versus time for varying experimental conditions.

As seen in Fig. 3.20, the temperature increases consistently to 25 degrees in the first 70 minutes. Once the syphon system is implemented, the temperature comes back down to 21 degrees within 30 minutes. The system's temperature was monitored for another 40 minutes in a settling period before LDV measurements were taken. During this period and for the rest of the experimental run, the temperature stayed constant at 21±0.5 degrees.

3.3.3 Inlet velocity profile

The main goals of measuring the inlet velocity were to get an estimate of the turbulence intensity at the inlet as well as the uniformity of the profiles. The inlet velocity profile was obtained by measuring the axial velocity on a line perpendicular to the inlet wall located 5 mm upstream of the pressure taps (in the square inlet section 15 mm downstream of the honeycomb exit, see Fig. 3.21). Ten evenly-spaced points were measured along this line, leading to points 6 mm apart.

The profile is presented in Fig. 3.22. The velocity profile is normalized by the bulk velocity through the rectangular inlet section (i.e., 2.60 m/s) and all points were re-sampled at 80 Hz which is the average sampling rate for the inlet. It can be seen in the figure that the profile is even with the percent difference between the points being on average less than 3%. The average turbulence intensity is 17%, which is within the expected values for the

55

flow. The high turbulence intensity is likely due to the high Reynolds number associated with the flow.
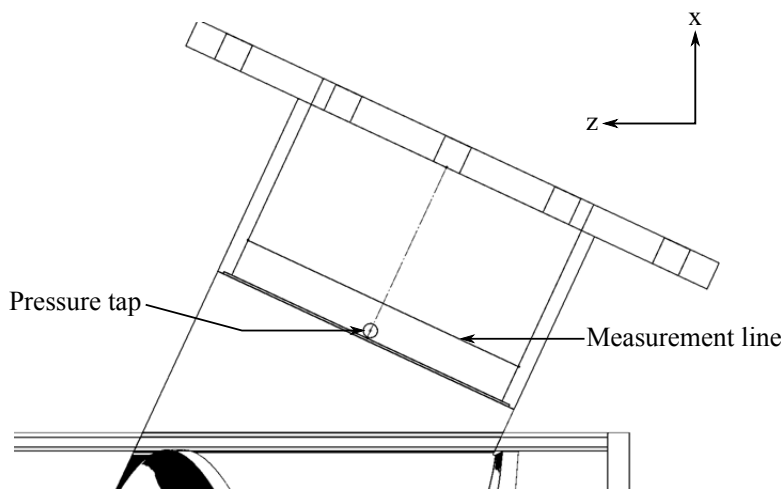
Figure 3.21: Measured location for the inlet velocity profile.
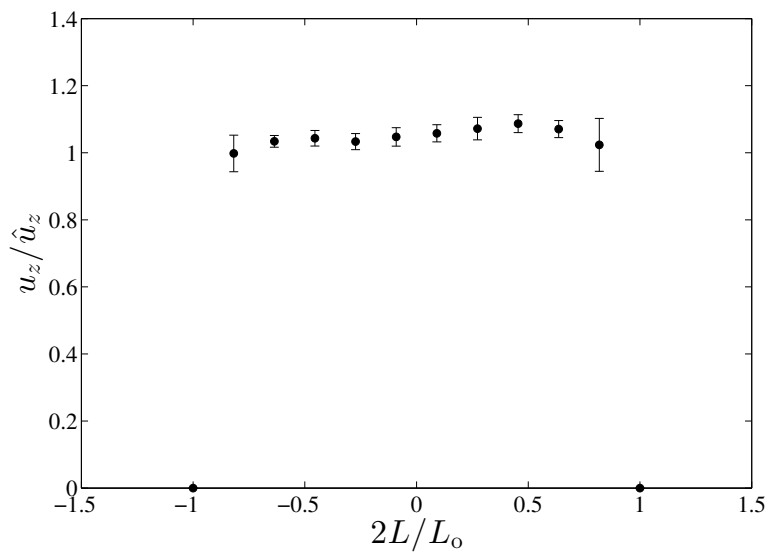
Figure 3.22: Inlet velocity profile.

3.4 Summary and conclusion

A swirl injector test rig was constructed in order to test the optimized swirl injector with
nose cone. The rig is composed of the reservoir, the pump, the gate valve, the circle-
to-rectangle transition, the flow conditioning elements, the swirl injector, the test section
and the flow meter. The whole system is a recirculating setup. The characterization of
the rig was done by observing the velocity drift in the test section and the temperature
fluctuations in the reservoir with and without cooling. The settling time for the system
was found to be 40 minutes. The inlet velocity profile was also measured and it was seen
that the turbulence intensity of the incoming flow was 17% with less than a 3% difference
in the uniformity of the flow. Figure 3.23 shows the full setup as seen in the laboratory.
The computer, power source, DAQ input and pressure sensor array are also seen to the
left of the table.

Figure 3.23: Full rig as seen in the laboratory.

Chapter 4

Flow characteristics of the optimized swirl injector with nose cone

This chapter discusses the impact of the inclusion of the nose cone on the swirl injector. This is explored via combined numerical simulation and experimental measurement using the facility described in Chapter 3.

4.1   Numerical model

The numerical domain, as seen in Fig. 4.1, is similar to the domain used in the numerical optimization of the swirl injector without the nose cone presented in Chapter 2. The two domains differ in that the present domain has a nose cone that terminates the swirl injector, as opposed to having a persistent annular cross-section, as in the case examined in Chapter 2. The present domain has a total of 8.1 million elements and 7.9 million nodes, with the same node density as for the optimization model. The boundary conditions for the nose cone model differ, however, from the model used in the numerical optimization; in the numerical optimization the boundaries were both pressure boundaries, whereas in the present model the inlet is a mass flow boundary condition and the outlet is a pressure outlet. This was done in order to achieve independence from the experimental results, since the boundary would have depended on a pressure measurement provided by the setup. Furthermore, the pressure measurement from the experiments would not be indicative of the average pressure through the cross-section, but rather the pressure at the wall, which is not constant since the flow is not fully developed. Therefore, if the average
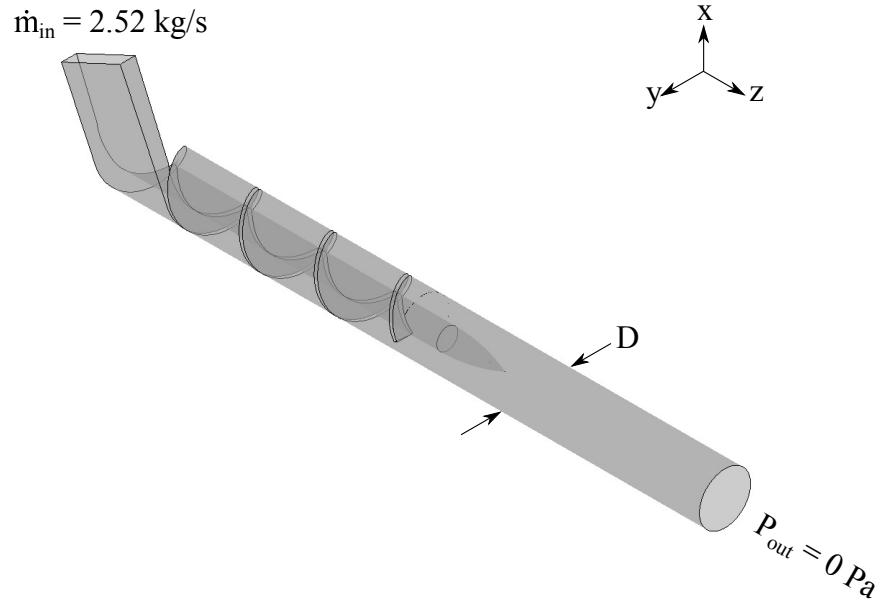
Figure 4.1: Computational domain used for the scaled model. The coordinate frame is also defined.

pressure was to be used as an inlet condition, it would result in higher velocities and, subsequently, higher pressure losses throughout the domain. The working fluid is water with density ρ and kinematic viscosity ν, with the same values as in Chapter 2. The flow is assumed incompressible, steady, and Newtonian, and thus is governed by the Navier-Stokes equations. The flow in the casing is highly turbulent, and thus, to facilitate the solution of the Navier-Stokes equations, we once more employ the Reynolds decomposition, $u_i = \bar{u}_i + u_i'$, where $\bar{u}$ is the time-averaged velocity component, u' is the fluctuating velocity component, and subscript i indicates the spatial direction of the component using standard index notation [50]. Employing the Reynolds decomposition and averaging over time yields the Reynolds Averaged Navier-Stokes (RANS), as in Chapter 2. The specific RANS model which was used is the k-ω shear stress transport (SST) turbulence model.
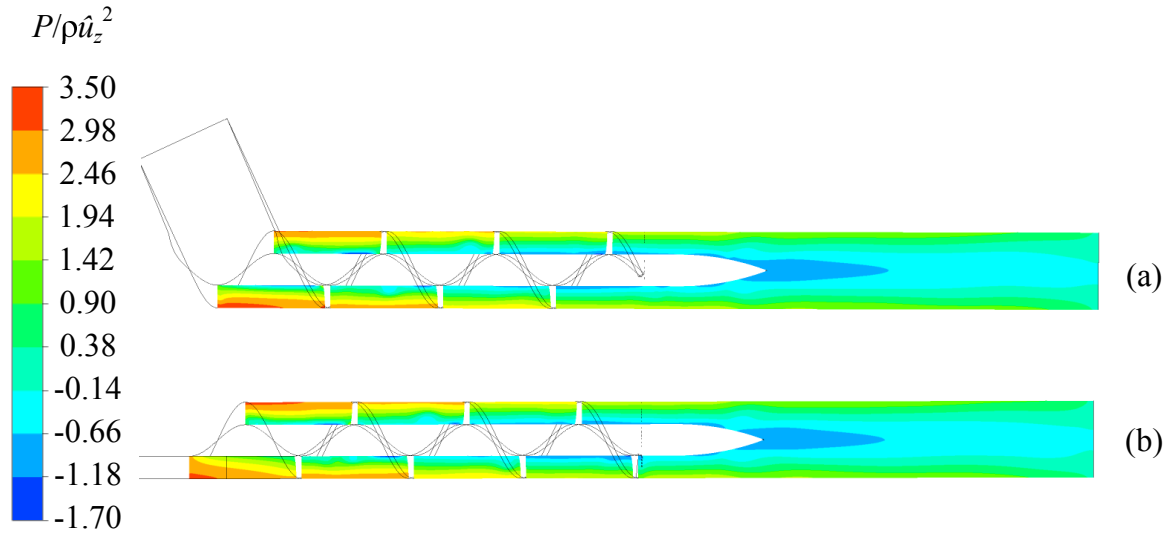
Figure 4.2: Normalized pressure contours for the (a) xz-plane (at y = 0) and the (b) zy-plane (at x = 0).

The pressure through the injector goes from high pressure to low pressure as the flow travels from the inlet region to the test section. Based on the contours in Fig. 4.2a and 4.2b, the pressure also varies from high to low from shroud to hub due to streamline curvature associated with the swirling motion. The higher pressure contours reduce in magnitude as the flow goes through the flighting, whereas the low pressure contours stay relatively similar throughout the injector. Past the tip of the nose cone, there is a low pressure region, which is co-located with the core of the vortex generated by the swirl injector. That is, though the nose cone is shaped to minimize flow separation, and thus wake size, there remains a low pressure region downstream of the nose cone due to the combined effects of flow separation (bluff body wake) and the swirl imparted on the flow. The pressure contours even out as the flow travels downstream of the edge of the flighting, as seen by the smaller radial gradients in the pressure further downstream.
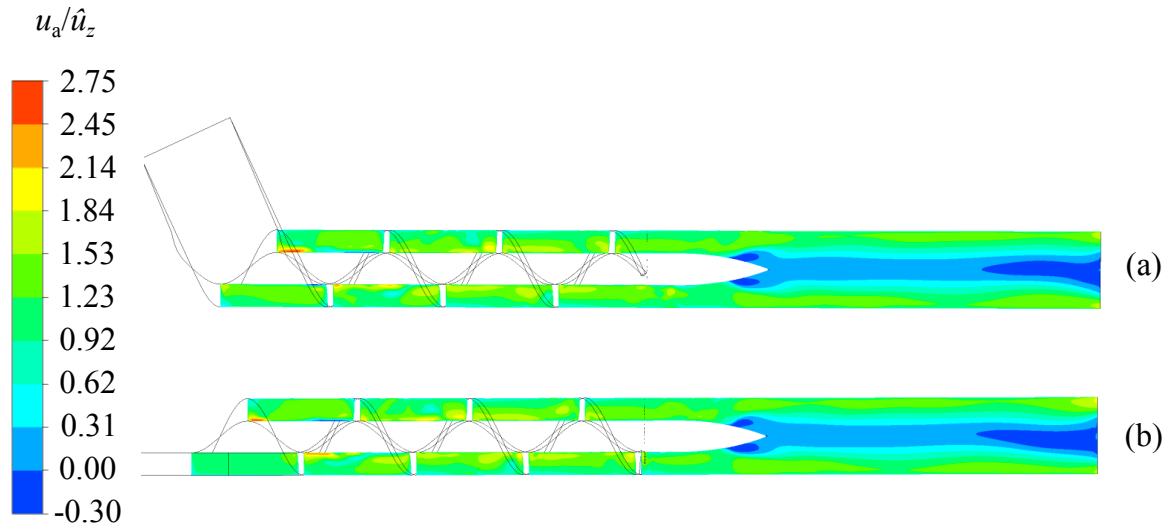
Figure 4.3: Normalized axial velocity contours for the (a) xz-plane (at y = 0) and the (b) zy-plane (at x = 0).
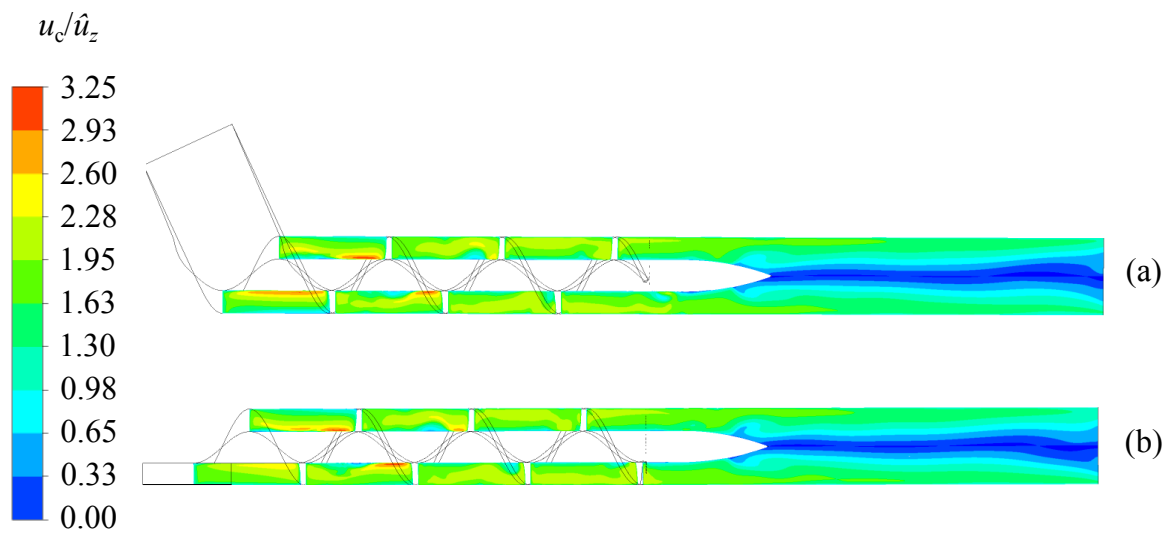

Figure 4.4: Absolute normalized circumferential velocity contours for the (a) xz-plane (at y = 0) and the (b) zy-plane (at x = 0).

The axial velocity is relatively constant through the injector. There are occasional regions of high velocity in the injector itself, namely near the hub potentially due to the previously discussed pressure gradient between the shroud and hub (see contours on Fig. 4.3a and 4.3b). At the tip of the nose, a region of negative axial velocity can be seen, indicative of flow separation and subsequent recirculation area in the wake of the nose cone. By comparing Fig. 4.3a and 4.3b, it can be seen that the recirculation zone goes around the nose cone. Immediately past the nose, a region of low velocity can be seen which is associated to the wake region behind the nose cone. Past the wake region, the low velocity core persists downstream at the center of the tube which is typical of swirling flows in pipes [70, 71]. The swirling of the flow not only affects the circumferential velocity component but also the axial velocity due to the pressure distribution. The lower pressure in the core slows the axial velocity at the core. There is also a negative velocity contour near the exit of the domain due to the proximity to the outlet. This is outside of the area of interest, however.

Like axial velocity, the circumferential velocity varies from high velocity at the hub to low velocity at the shroud, see Fig. 4.4a and 4.4b, which is, once more, caused by the pressure gradient. It can also be seen that the circumferential velocity is starting to overtake the axial velocity as the flow travels through the injector, indicative of a strong swirl. On the nose cone there are small patches of low circumferential velocity near where the center of the recirculation zone would be located which is expected of vortices.As the flow travels through the injector, the distribution of the velocity becomes more even. Once the flow travels past the nose, it can be seen that there is a section of low velocity at the center of the tube, similar to a vortex [70, 71].

As seen in Fig. 4.5, the swirl number decreases as we go further downstream. This loss of swirl energy is consistent with what was seen in the numerical optimization. As before, the circumferential velocity degrades as it gets further from the edge of the flighting. The swirl numbers at D0.5 are within 5.6% of the value computed in optimization study. Considering that the geometries and boundary conditions between the two models are quite different, there is relatively good agreement between the swirl number. It should be noted that the diameters mentioned in the comparison between the two numerical models are at the physical location as seen on the experimental model (i.e., not offset by 5 mm).

In Fig. 4.6, the evolution of the axial and circumferential velocity axisymmetry is investigated. It can be seen that in both components of velocity that the uniformity is improved as the flow goes downstream. Compared to the previous model, the nose cone models axisymmetry is worse in both the axial and circumferential velocities. In the optimization study's model, the axial and circumferential axisymmetry values are 5.4% and 6.1%, respectively. Whereas, with the nose cone model the values are 9.5% and 13%
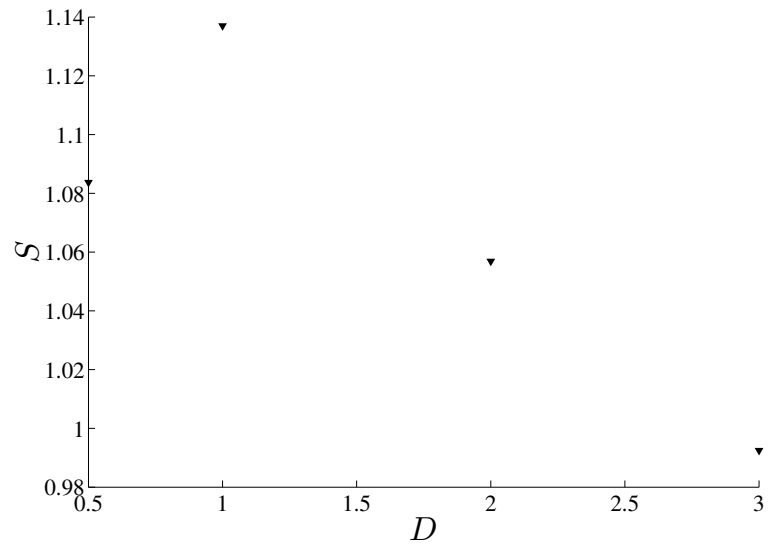
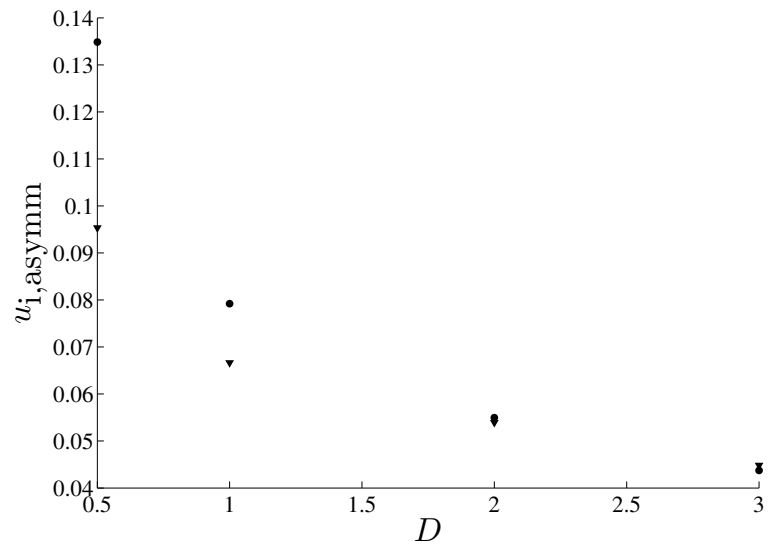Figure 4.5: Evolution of swirl number downstream of the edge of the flighting.

Figure 4.6: Evolution of axial (circular symbol) and circumferential (triangular symbol) axisymmetry downstream of the edge of the flighting.

for the axial and circumferential velocities, respectively. The discrepancy is caused by the presence of the wake region in the nose cone model (recall that the optimization model did not have a termination of the annular region). The wake region starts at the nose cone and propagates downstream into the test section.

4.1.1 Axial and circumferential velocity profiles in the injector

The axial and circumferential velocity profiles from D0.5 to D3 and the pressure difference between the D0.5 and D3 were compared between the numerical and experimental results. The velocity measurements were re-sampled at 106 Hz which is the average frequency of all the measured points.

As previously mentioned in Chapter 3, the diameters referred to in the comparison between the numerical and experimental velocity profiles are the offset diameters (i.e.,the actual location where the measurements were taken). Figures 4.7a to 4.7d compare the axial velocity profile along the x-axis. In Fig. 4.7a to 4.7b, the axial profiles have peaks near $r/r_o = \pm 0.75$ which is typical of annular pipe flows. The magnitude of the average axial velocity seems to decrease as the flow goes from D0.5 to D1, possibly due to the increasing cross-sectional area encountered by the flow. Evident in Fig. 4.7a to 4.7d is the high degree of scatter in the experimental measurements, particularly near the hub and the center of the tube. This discrepancy is due to the presence of the wake region near the nose cone which is the propagated downstream. Generally speaking, the axial velocity peaks increase as the the flow travels downstream.

At D0.5, the agreement between the experimental and the numerical results is good when investigating the points less than $r/r_0 = 0$. There is a large discrepancy (on average 70%) in the points nearest to the hub, likely due to the wake of the nose cone. The average velocities for the experimental case are on average 41% far from the numerical results at D1 which is quite a large discrepancy. The numerical results are 7% higher than the experimental result which are lower due to the presence of the wake region which causes a decrease in velocity. It should be noted also that in both the D0.5 and D1 profiles there are points between $r/r_0 = \pm 0.5$ and $r/r_o = \pm 0.75$ which have large error bars (about 55%). This is likely due to the point being located in the shear layer roll-up region which has a large amount of fluctuation. Downstream of the nose cone (D2; Figure 4.7c), the experimental flow profiles agree well with the numerical results except at the points nearest to the middle of the tube. This is largely due to an accumulation of air bubbles in the middle of the tube in the experiment. The air bubbles tend to migrate towards the low pressure at the center of the vortex induced by the swirl injector. The air bubbles cause

Figure 4.7: Axial velocity profiles for the experimental case (asterisk symbol) compared to the numerical results (circular symbol). The profiles were taken for the (a) D0.5 and (b) D1.

Figure 4.7 (cont.): Axial velocity profiles for the experimental case (asterisk symbol) compared to the numerical results (circular symbol). The profiles were taken for the (c) D2 and (d) D3.

Figure 4.8: Circumferential velocity profiles for the experimental case (asterisk symbol) compared to the numerical results (circular symbol). The profiles were taken for the (a) D0.5 and (b) D1.

(c)

(d)
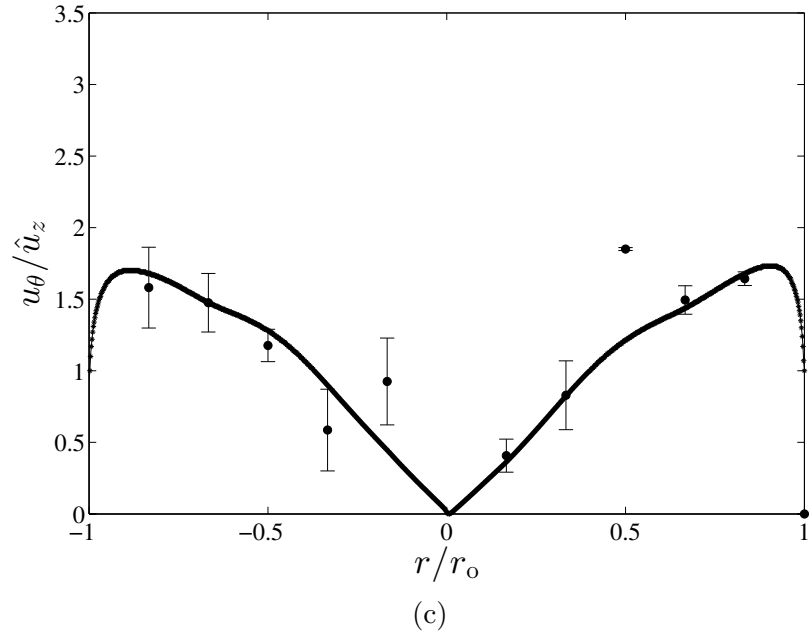
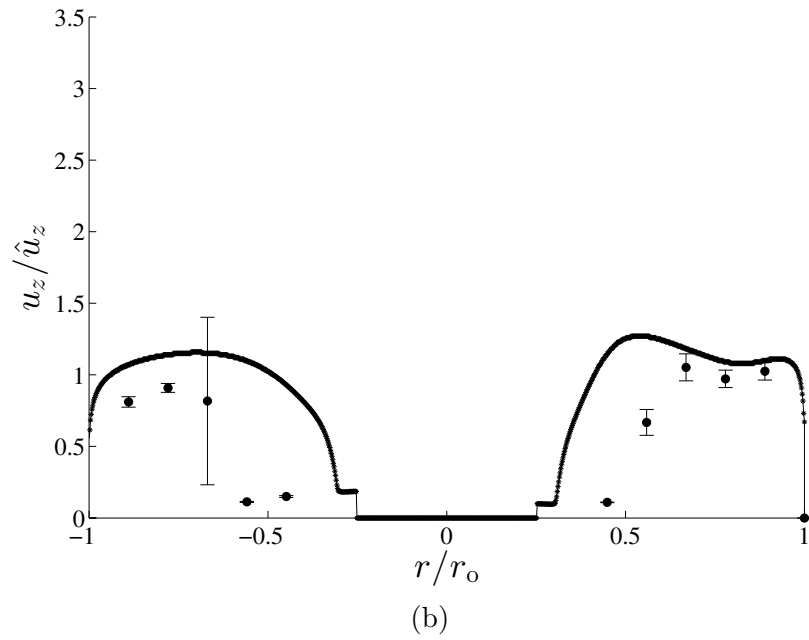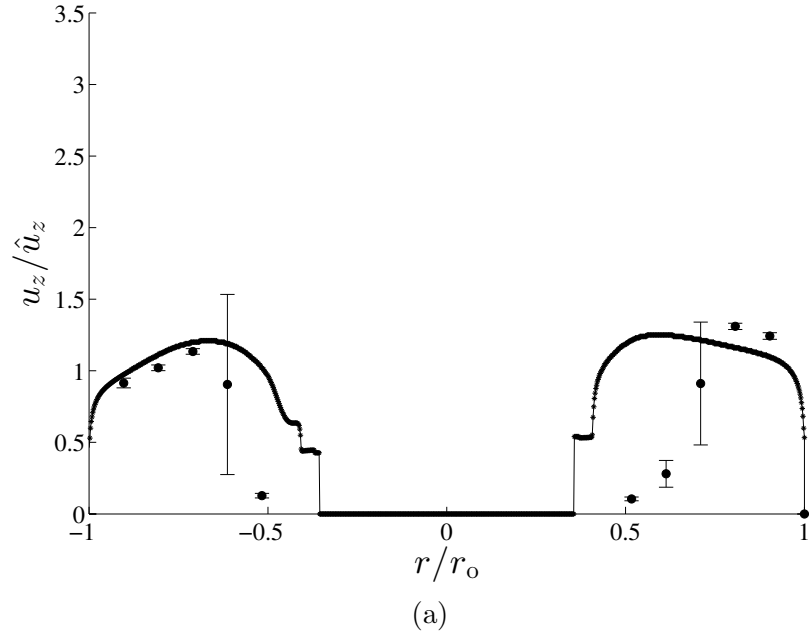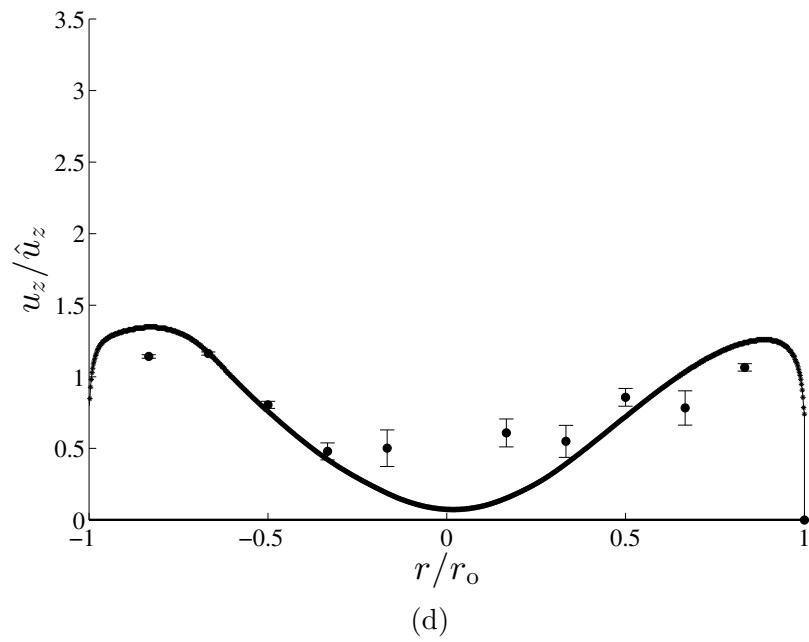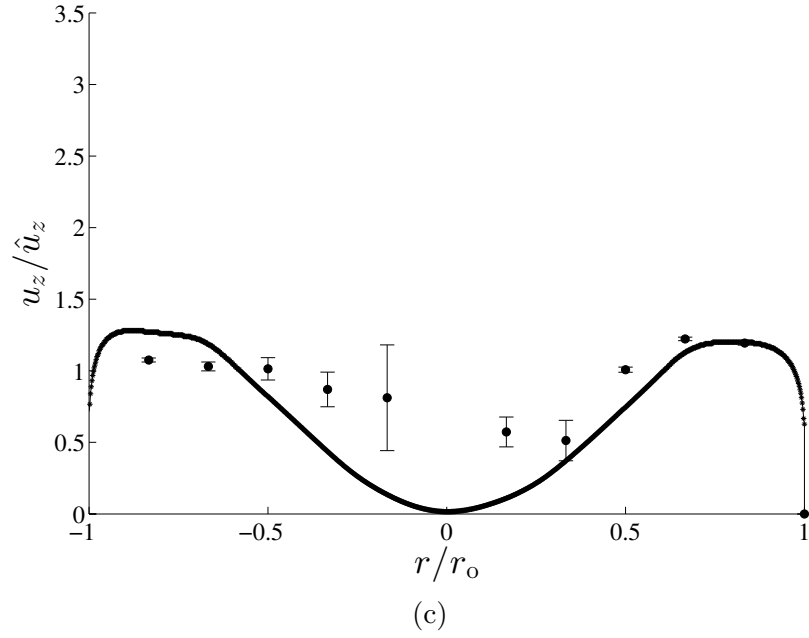Figure 4.8 (cont.): Circumferential velocity profiles for the experimental case (asterisk symbol) compared to the numerical results (circular symbol). The profiles were taken for the (c) D2 and (d) D3.
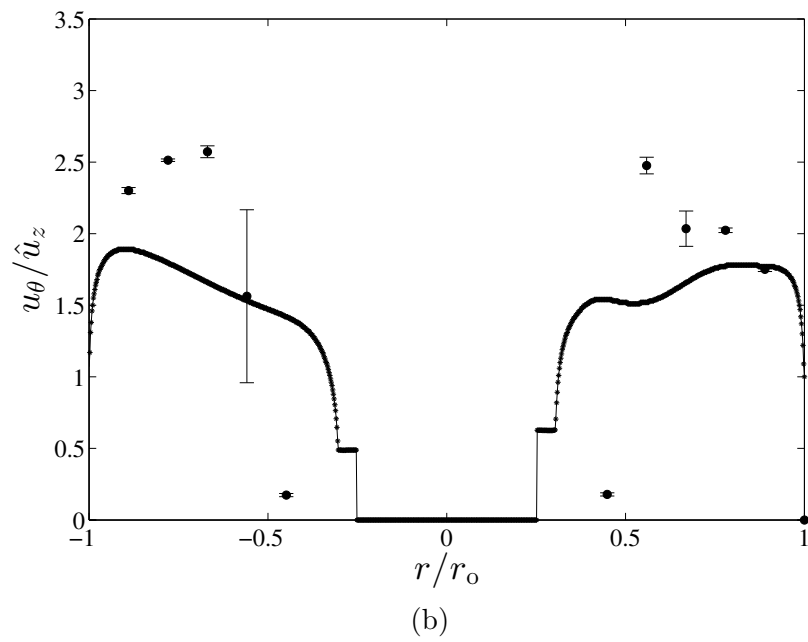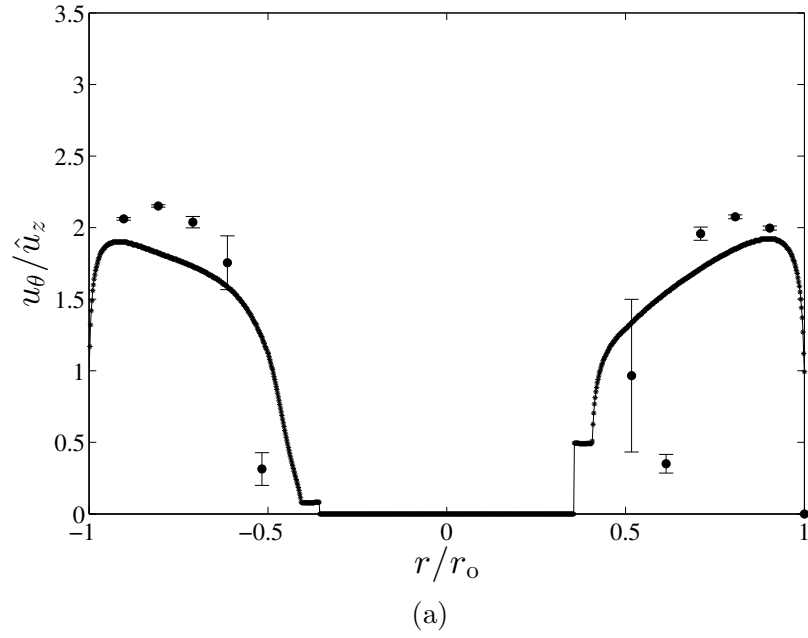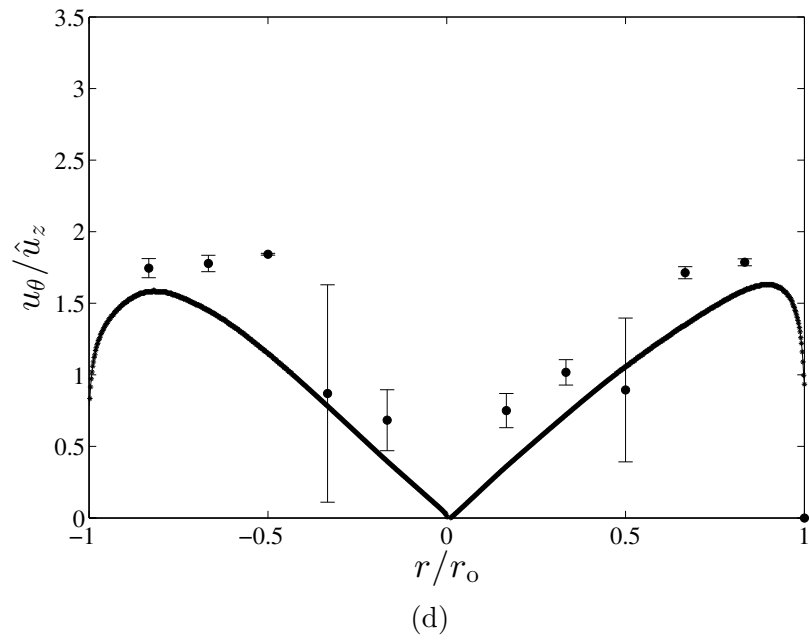
the LDV laser beams to be deflected off of them causing erroneous measurements. Another cause of this discrepancy may be the downstream propagation of the wake region which is not well predicted by the numerical simulation. Good agreement can also be seen in D3 between the numerical and experimental profiles with similar discrepancies in the middle points caused by air bubble accumulation and wake propagation.

Figures 4.8a to 4.8d shows the results for the circumferential velocity profiles for the D0.5, D1, D2 and D3 planes. The circumferential velocity profiles at the D0.5, and D1 planes are similar to their axial velocity counterpart due to the similar velocity profile shapes. The main difference between the axial and circumferential profiles is the higher velocity magnitude of the circumferential velocity. The higher magnitude is caused by the strong swirl provided by the swirl injector. Referring back to the numerical simulation of the nose cone model, a strong swirl was predicted and therefore would cause the circumferential velocity to be higher in magnitude than the axial velocity. There also seems to be a slight increase in the circumferential velocity as the flow propagates downstream.

The experimental profiles for D2 and D3 profiles seem to be very close together. The profiles for circumferential velocity at D2 and D3 are also evocative to a turbulent swirling flow through a pipe, similar to the axial velocity profiles. Comparing the axial and circumferential profiles it can be seen that the circumferential velocity is much higher than the axial velocity, indicative of a strong swirling flow and a high swirl number value.

As seen in the Fig. 4.8a to 4.8d, the circumferential velocity profiles have a discrepancy between the numerical and experimental results. The higher velocity magnitude of the circumferential component causes a higher LDV bias error. The error on the LDV measurement is due to the inherent bias of detecting high velocity particles through the probe volume, this is highlighted when there are different sampling rates, which is the case with the current profiles [67, 68]. Even with the re-sampling there still is a significant amount of discrepancy. This explains why the numerical velocity magnitudes are lower than the experimental results. The experimental profiles at D0.5 and D1 have similar shapes to the numerical profiles, though there is a sharper decline observed in the experimental profile at the points nearer to the hub. This is likely due to the high turbulence near the hub which is under-predicted by the numerical solution. The shape of the experimental circumferential velocity profiles at D2 and D3 match the numerical results. Once more, the most notable exceptions in the profile shape are the two middle points which due to the accumulation of of air bubbles in the center of the tube.
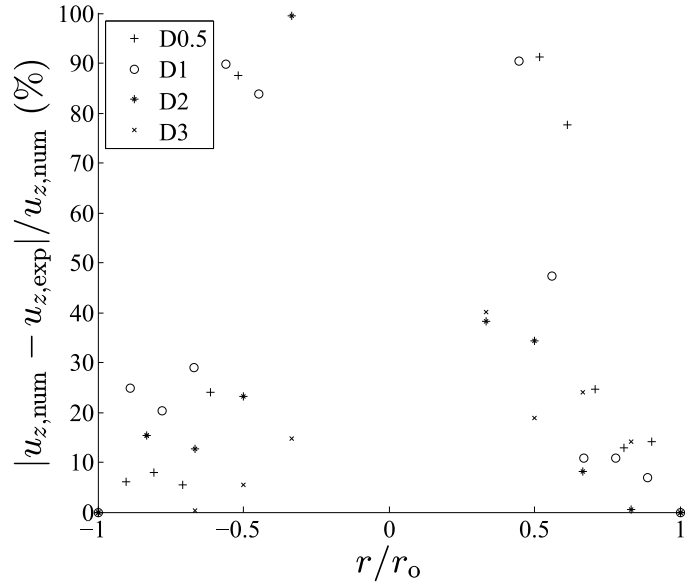
(a)
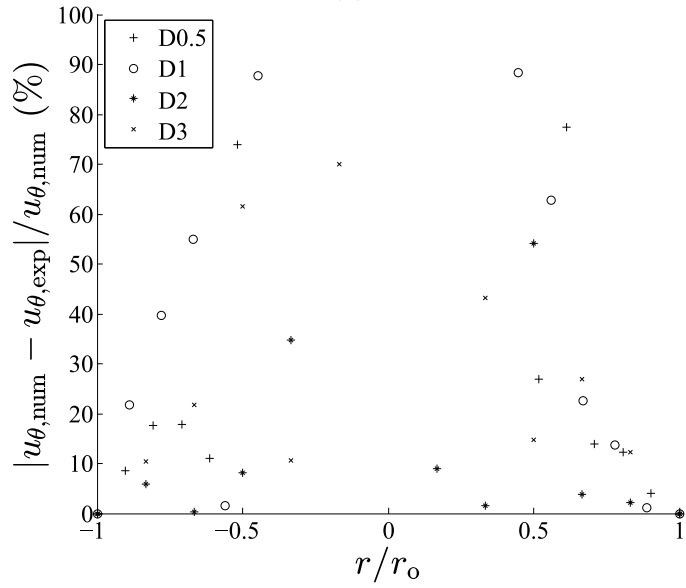
(b)

Figure 4.9: Percent difference between the numerical and experimental results for the (a) axial and (b) circumferential velocities. It should be noted that the numerical results serve as the point of comparison (i.e. true value).

The agreement between the numerical and the experimental results can be elucidated by taking a more quantitative look at the percent difference between the numerical and experimental results, as seen in Figs. 4.9a and 4.9b. It should be noted the average values of the experimental results are used in the comparison (i.e. the uncertainty is not taken into consideration) and that certain points, particularly near $r/r_o = 0$, are out of the scale of the graph. Generally, the percent difference increases towards $r/r_o = 0$ for both the axial and circumferential velocity. There is a particularly large discrepancy for the D2 and D3 profiles at middle points, likely due to the accumulation of air bubbles. The average percent differences for axial velocity for the D0.5, D1, D2, and D3 profiles are 35%, 41%, 114%, and 59% respectively. Looking at the average percent differences it could be concluded that there is a large difference in the results for the D2 and D3 profiles, though this average is skewed by the large (300% to 500%) difference towards the middle of the cross-section. The average percent differences for circumferential velocity for the D0.5, D1, D2, and D3 profiles are 26%, 39%, 22%, and 38% respectively. Overall, there is a 62% and 31% difference for the axial and circumferential velocity respectively. The larger difference in the axial velocity can be justified by the large spikes in the points near the middle of the tube as well as the points near the wake. Without the middle points and the wake points, the average difference for the axial velocity is 15%, whereas with the circumferential velocity there is a 31% difference. It can therefore be concluded that the axial velocity has a better agreement with the numerical results, if the wake and middle points are neglected. Whereas, the circumferential velocity has an overall better agreement with the numerical results but has a poor correlation compared to the axial velocity when neglecting the wake and middle points.

4.1.2   Pressure through the injector

As discussed in Chapter 3, the diameters discussed in the following section are the physical locations (i.e., no 5 mm offset). Figure 4.10 shows the numerical and experimental results for the measured pressure. In order to make the pressures comparable between the experimental and numerical results, the pressure at D3, for each result set, is subtracted from the results from each set. Based on Fig. 4.10, the pressure increases at D1 before going back down below the D0.5 value. The increase in pressure is likely due to the change of cross-sectional area and the flow impinging onto the nose cone; the cross-sectional area increases as the flow travels over the nose cone, the larger cross-section slows the flow (locally) and causes the pressure to increase. As the flow exits the injector, a part of the flow impinges onto the nose cone. The eddies generated by the impinging flow increased the pressure locally at D1. There is a notable difference (about 40%) between the pressures at the D1 cross-section between the numerical and experimental, likely due an under-prediction of the wake region in the numerical simulation. The eddies caused by the flow impinging on the nose cone are not being predicted as accurately as is necessary to match the pressures. A direct numerical simulation (DNS) would likely be able to more accurately predict this
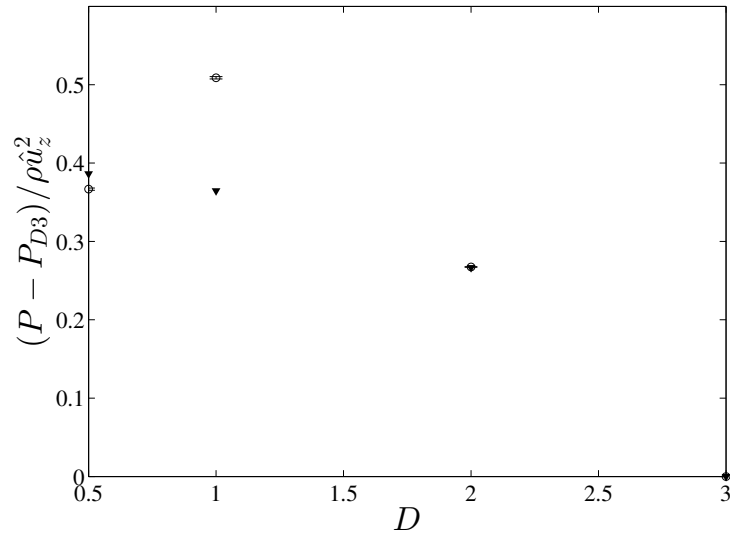
Figure 4.10: Measured pressure versus number of diameters downstream for the experimental (circular symbol) and numerical (triangular symbol) results. Note that the pressure is normalized by the bulk velocity (i.e., 1.25 m/s).
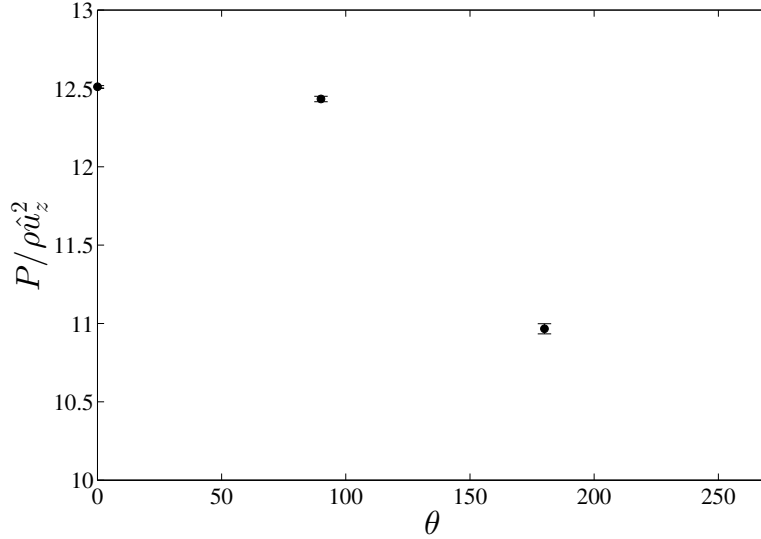
Figure 4.11: Circumferential pressure distribution at D0.5 which was measured experimentally. Note that the pressure is normalized by the bulk velocity (i.e., 1.25 m/s) and that θ is the circumferential location.

but the computational resources to do such a simulation are currently unavailable since the required resources are proportional to the Reynolds number.

The measured pressure drop between D0.5 and D3 for the experiments was 0.566 kPa and the numerical simulation yielded a pressure drop of 0.597 kPa. There is a 5% difference between the two values, which can be justified by the difference in boundary conditions. The outlet of the simulation is a an average 0 Pa pressure outlet, whereas in reality there is most likely a pressure head due to the downstream bends in the piping. Thus the pressure loss is less in the experiments than in the numerical solution.

The circumferential distribution of the pressure can be seen for the D0.5 can be seen in Fig. 4.11. The $\theta = 0$ point is located in the negative y-direction and all subsequent points are encountered in the counter-clockwise direction. The average percent difference between the points for the experimental and numerical results are 7% and 4% respectively. The 3% difference between the two results is acceptable considering, once again, the differences between the boundary conditions.

73

4.1.3 A note on scaling

The Π_1 value, obtained using Eq. 1.10, for the optimization model is $7.87 * 10^{-4}$ whereas for the nose cone model the value is 21.5. The discrepancy between the models is due to the use of the pump in the nose cone model. The pump outputs high pressure at low flow rates, therefore skewing the Π_1 value. In spite of this discrepancy, the general dynamics of the flow stay similar, based on the result comparison between the optimization model and the nose cone model.

4.1.4 Conclusion

The flow through a swirl injector with a nose cone was investigated in this chapter. A numerical model was created using the same node density as the optimization model. The boundary conditions were set to a mass flow inlet and a 0 Pa pressure outlet. The k-ω SST turbulence model was again used to predict the turbulence. From the results of the simulation, it was determined, by investigating pressure contours, that the pressure would go from high to low as the flow traveled downstream. The pressure contours also showed that there is a low pressure zone immediately after the nose cone due to the imparted swirl. The axial velocity contours showed that there are recirculation zones at the nose cone, insinuating a separation bubble at the nose cone. The circumferential velocity contours showed the evolution of the circumferential velocity as it went from high within the injector to low in the test section, similar to the axial velocity. The swirl number and the axisymmetry metrics between the nose cone model and the optimization model were in good agreement in spite of the differences in boundary conditions.

The axial and circumferential measurements from the experimental campaign were compared to the nose cone model results. The shapes of the experimental results generally showed good agreement with the numerical results with the exception of the points nearest to the nose cone. As for the pressure difference, the experimental results were within 5% of the numerical results, which is justified when considering the difference in boundary conditions. There is a spike in pressure at D1 which isn't seen in the numerical results. A DNS approach might be able get better results.

Chapter 5

Conclusions and summary

A numerical and experimental investigation of a swirl injector was performed. Numerical optimization of the swirl injector design was performed, as well as characterization of the optimized geometry in a realistic configuration incorporating a nose cone. An experimental setup was also designed and commissioned to aid in numerical validation and to enable future studies. The pressures and velocities of the experimental setup were compared with numerical simulations. The findings of both the numerical and experimental investigations will be summarized in the following sections.

5.1 Numerical optimization of a vaneless swirl injector

The swirl injector design was numerically investigated in order to develop geometric design guidelines for efficient operation. To ensure efficient operation of a water turbine employing the vaneless swirl injector, the flow downstream of the injector should be relatively uniform in the rotor plane, have high swirl, and the pressure losses should be minimized. A series of swirl injector designs with varying pitch angles and number of revolutions of the swirl injector were considered.

In general, the velocity and pressure fields within the swirl injector became increasingly axisymmetric as the number of revolutions and the pitch angle increased. Increasing either variable increased the overall length of the injector, thus leading to a greater flow development distance, which improved flow axisymmetry. The swirl imparted to the fluid and the pressure losses through the device increased with increasing number of revolutions

and decreasing pitch angle. As the number of revolutions increases, the length of the rifling increased, leading to a larger swirl component, but also increased the surface area, which increased the pressure losses. Decreasing pitch angle increased the swirl number, thus increasing the energy available for the turbine to extract, but also rapidly increased the losses through the device.

An objective function was constructed from four key characteristics at the rotor plane; axisymmetry of the axial flow, axisymmetry of the circumferential flow, the pressure losses from the inlet to the rotor plane, and the swirl number. The first three metrics were to be minimized, while the latter was to be maximized. The optimization study results indicated that the objective function is much more sensitive to the pitch angle of the swirl injector than to its number of revolutions. The objective function was then optimized using a line search method. A pitch angle of 25° with 4 revolutions was found to be optimal. In practice, however, overall device length is a concern. Given the relative insensitivity of the device performance on the number of revolutions, it is recommended that the pitch angle be set and overall device length be controlled via the number of revolutions.

5.2 Characterization of the optimized swirl injector geometry with an attached nose cone

The optimized version of the injector was simulated with a nose cone. The pressure contours showed the presence of a low pressure region immediately after the nose cone. The axial velocity contours showed a recirculation zone on the nose cone. The circumferential velocity contours showed the evolution from high to low of the circumferential velocity. The results were similar to the model used in the optimization study, based on the swirl number and the axisymmetry metrics. The major differences between the two models were the presence of a wake region as well as the mass flow boundary condition in the nose cone model. This wake region caused recirculation zones which caused minor differences in the metrics between the models.

The numerical results were validated by the experimental results for the axial and circumferential velocity profiles. The shapes of the experimental and numerical profiles match for the most part with exception to the points closest to the hub or the vortex core. There is a 5% difference between the numerical and experimental pressure differences, due to the difference in boundary conditions. There is a spike in pressure at D1 in the experimental which isn't seen in the numerical simulation. The only way this can be resolved by doing a DNS simulation which, at the moment, is too computationally expensive.

Chapter 6

Recommendations

From the results obtained in the study, the author makes the following recommendations with respect to future numerical and experimental studies.

6.1 Numerical study

1. Ultimately, the goal is to be able to simulate the swirl injector and rotor assembly. In order to do this, the rotor by itself should be simulated with the inlet condition mimicking the swirling flow coming out of the swirl injector. The domain for the simulation will be a straight pipe, with 1 pipe diameter in front and 5 diameters behind the rotor.

2. With the rotor simulated separately, the final step would be to couple the two simulations together. The outlet condition from the injector will be used as an inlet condition for the rotor simulation.

3. An optimization study on the rotor geometry should be performed in order to find the optimal shape for the rotor.

6.2 Experimental study

1. The model which is currently used is small, therefore amplifying the uncertainties due to the resolution of the traverse. A 0.1016 or 0.1524 m model would provide

better results with lesser relative uncertainty. Upgrading to a 0.1016 or 0.1524 m pipe would require connecting the setup to the constant head tank in the UW Fluid Mechanics Laboratory since the flow rates would be a lot higher than the ones the pump would be able to output. Furthermore, if the pump was used, the head loss from transitioning from 0.0508 to 0.1524 m would be quite large. The constant head tank has a maximum head of 4.2 m, which is sufficient for the purposes of the experiments.

2. In order to get a clearer picture of the flow (i.e. one with more spacial resolution) and perhaps better characterize the flow, particle image velocimetry (PIV) should be done on the test section. In order to be able to do PIV, a rectangular transparent box should be fitted over the test section and filled with fluid with the same index of refraction as the pipe and the box. This will allow the high speed cameras to capture the flow without the image being distorted by the curvature of the pipe wall.

3. A 3D printed rotor should be installed and tested. The design of the rotor would be based on the results of previously mentioned numerical optimization study. A magnetic braking system would also be installed in order to control the rotational speed of the rotor. The goal of this will be to validate the numerical study.

References

[1] A. Ansar, B. Flyvbjerg, A. Budzier, and D. Lunn, "Should we build more large dams? The actual costs of hydropower megaproject development," *Energy Policy*, vol. 69, pp. 43–56, 2014.

[2] C. Wolfram, O. Shelef, and P. J. Gertler, "How will energy demand develop in the developing world?," tech. rep., National Bureau of Economic Research, 2012.

[3] L. Kosnik, "The potential of water power in the fight against global warming in the US," *Energy Policy*, vol. 36, no. 9, pp. 3252–3265, 2008.

[4] M. Farriz, H. Boejang, M. Masjuri, M. Aras, N. Razik, S. Mate, and K. Sopian, "Evolution of simple reaction type turbines for pico-hydro applications," *Jurnal Teknologi*, vol. 77, no. 32, pp. 1–9, 2015.

[5] P. Duquesne, Y. Maciel, and C. Deschênes, "Investigation of flow separation in a diffuser of a bulb turbine," *ASME J. Fluids Eng.*, vol. 138, no. 1, pp. 011102–011102–9, 2015.

[6] O. Paish, "Small hydro power: technology and current status," *Renewable and Sustainable Energy Reviews*, vol. 6, no. 6, pp. 537–556, 2002.

[7] E. M. Wilson, "Small-scale hydroelectricity," *Energy Policy*, vol. 19, no. 8, pp. 787–791, 1991.

[8] S. Kato, N. Hoshi, and K. Oguchi, "Small-scale hydropower," *Industry Applications Magazine, IEEE*, vol. 9, no. 4, pp. 32–38, 2003.

[9] L. Kosnik, "The potential for small scale hydropower development in the US," *Energy Policy*, vol. 38, no. 10, pp. 5512–5519, 2010.

[10] D. Benzon, A. Židonis, A. Panagiotopoulos, G. Aggidis, J. Anagnostopoulos, and D. Papantonis, "Impulse turbine injector design improvement using computational fluid dynamics," *ASME J. Fluids Eng.*, vol. 137, no. 4, pp. 041106–041106–9, 2015.

[11] D. De Montmorency, "High Reaction Turbines, Bridging the Gap between Francis and Kaplan," in *Waterpower 2007*, 2007.

[12] NORCAN, "NORCAN Hydraulic Turbine Inc. website." `http://www.norcanhydro.com/`. Accessed: 2016-07-25.

[13] B. Leyland, *Small Hydroelectric Engineering Practice*. CRC Press, 2014.

[14] A. Arasu, *Turbo Machines, 1E*. Vikas Publishing House Pvt Limited, 2009.

[15] S. A. Korpela, *Principles of turbomachinery*. Hoboken, N.J.: Wiley, 2011.

[16] D. K. Okot, "Review of small hydropower technology," *Renewable and Sustainable Energy Reviews*, vol. 26, pp. 515 – 520, 2013.

[17] G. Ardizzon, G. Cavazzini, and G. Pavesi, "A new generation of small hydro and pumped-hydro power plants: Advances and future challenges," *Renewable and Sustainable Energy Reviews*, vol. 31, pp. 746 – 761, 2014.

[18] O. Paish, "Small hydro power: technology and current status," *Renewable and Sustainable Energy Reviews*, vol. 6, no. 6, pp. 537 – 556, 2002.

[19] S. L. Dixon, *Fluid mechanics and thermodynamics of turbomachinery*. Boston: Butterworth-Heinemann, 2005.

[20] V. Volshanik and A. Etkin, "The "ideal" guide vanes for a reaction turbine," *Hydrotechnical Construction*, vol. 28, no. 9, pp. 540–546, 1994.

[21] T. Setoguchi, S. Santhakumar, M. Takao, T. Kim, and K. Kaneko, "Effect of guide vane shape on the performance of a Wells turbine," *Renewable Energy*, vol. 23, no. 1, pp. 1 – 15, 2001.

[22] A. Mohseni, E. Goldhahn, R. A. Van den Braembussche, and J. R. Seume, "Novel IGV designs for centrifugal compressors and their interaction with the impeller," *Journal of Turbomachinery*, vol. 134, no. 2, p. 021006, 2012.

[23] L. Ferro, L. Gato, and A. Falcão, "Design and experimental validation of the inlet guide vane system of a mini hydraulic bulb-turbine," *Renewable Energy*, vol. 35, no. 9, pp. 1920 – 1928, 2010.

[24] L. Tan, S. Cao, and S. Gui, "Hydraulic design and pre-whirl regulation law of inlet guide vane for centrifugal pump," *Science China Technological Sciences*, vol. 53, no. 8, pp. 2142–2151, 2010.

[25] K. Alexander, E. Giddens, and A. Fuller, "Axial-flow turbines for low head microhydro systems," *Renewable Energy*, vol. 34, no. 1, pp. 35–47, 2009.

[26] W. Chan, Y. Wong, S. Yu, and L. Chua, "A computational study of the effects of inlet guide vanes on the performance of a centrifugal blood pump," *Artificial Organs*, vol. 26, no. 6, pp. 534–542, 2002.

[27] F. S. A. Bracken and M. C. Lucas, "Potential impacts of small-scale hydroelectric power generation on downstream moving lampreys," *River Research and Applications*, vol. 29, no. 9, pp. 1073–1081, 2013.

[28] M. Larinier, "Fish passage experience at small-scale hydro-electric power plants in france," *Hydrobiologia*, vol. 609, no. 1, pp. 97–108, 2008.

[29] G. F. Čada, "The Development of Advanced Hydroelectric Turbines to Improve Fish Passage Survival," *Fisheries*, vol. 26, no. 9, pp. 14–23, 2001.

[30] G. Čada, J. Loar, L. Garrison, J. Fisher, Richard, and D. Neitzel, "Efforts to reduce mortality to hydroelectric turbine-passed fish: Locating and quantifying damaging shear stresses," *Environmental Management*, vol. 37, no. 6, pp. 898–906, 2006.

[31] N. Spring, "Fish-friendly Hydro Turbine," *Power Engineering*, vol. 114, no. 3, pp. 48–51, 2010.

[32] M. S. Iliescu, G. D. Ciocan, and F. Avellan, "Analysis of the cavitating draft tube vortex in a francis turbine using particle image velocimetry measurements in two-phase flow," *Journal of Fluids Engineering*, vol. 130, no. 2, p. 021105, 2008.

[33] Z. Deng, G. Guensch, C. McKinstry, R. Mueller, D. Dauble, and M. Richmond, "Evaluation of fish-injury mechanisms during exposure to turbulent shear flow," *Canadian Journal of Fisheries and Aquatic Sciences*, vol. 62, pp. 1513–1522, 2005.

[34] Z. Deng, T. J. Carlson, G. R. Ploskey, M. C. Richmond, and D. D. Dauble, "Evaluation of blade-strike models for estimating the biological performance of Kaplan turbines," *Ecological Modelling*, vol. 208, pp. 165–176, Nov. 2007.

[35] J. Laghari, H. Mokhlis, A. Bakar, and H. Mohammad, "A comprehensive overview of new designs in the hydraulic, electrical equipments and controllers of mini hydro power plants making it cost effective technology," *Renewable and Sustainable Energy Reviews*, vol. 20, pp. 279–293, 2013.

[36] J. S. Anagnostopoulos and D. E. Papantonis, "Optimal sizing of a run-of-river small hydropower plant," *Energy Conversion and Management*, vol. 48, no. 10, pp. 2663–2670, 2007.

[37] J. I. Perez-Diaz and J. Fraile-Ardanuy, "Neural networks for optimal operation of a run-of-river adjustable speed hydro power plant with axial-flow propeller turbine," in *Control and Automation, 2008 16th Mediterranean Conference on*, pp. 309–314, IEEE, 2008.

[38] A. Williams and R. Simpson, "Pico hydro–reducing technical risks for rural electrification," *Renewable Energy*, vol. 34, no. 8, pp. 1986–1991, 2009.

[39] K. Alexander and E. P. Giddens, "Microhydro: cost-effective, modular systems for low heads," *Renewable Energy*, vol. 33, no. 6, pp. 1379–1391, 2008.

[40] S. Williamson, B. Stark, and J. Booker, "Low head pico hydro turbine selection using a multi-criteria analysis," *Renewable Energy*, vol. 61, pp. 43–50, 2014.

[41] P. Singh and F. Nestmann, "Experimental optimization of a free vortex propeller runner for micro hydro application," *Experimental Thermal and Fluid Science*, vol. 33, no. 6, pp. 991–1002, 2009.

[42] J. Chen, H. Yang, C. Liu, C. Lau, and M. Lo, "A novel vertical axis water turbine for power generation from water pipelines," *Energy*, vol. 54, pp. 184–193, 2013.

[43] S.-R. Huang, Y.-H. Ma, C.-F. Chen, K. Seki, and T. Aso, "Theoretical and conditional monitoring of a small three-bladed vertical-axis micro-hydro turbine," *Energy Conversion and Management*, vol. 86, pp. 727–734, 2014.

[44] J. Wang, Q. Li, and N. Muller, "Mechanical and optimization analyses for novel wound composite axial impeller," in *ASME 2009 International Mechanical Engineering Congress and Exposition*, pp. 49–53, American Society of Mechanical Engineers, 2009.

[45] J.-f. Wang, J. Piechna, and N. Mueller, "A novel design of composite water turbine using cfd," *Journal of Hydrodynamics, Ser. B*, vol. 24, no. 1, pp. 11–16, 2012.

[46] J. Wang, J. Piechna, and N. Müller, "A novel design and preliminary investigation of composite material marine current turbine," *Archive of Mechanical Engineering*, vol. 58, no. 4, pp. 355–366, 2011.

[47] A. W. Turnpenny, M. Davis, J. Fleming, and J. Davies, "Experimental studies relating to the passage of fish and shrimps through tidal power turbines.," 1992.

[48] A. W. Turnpenny, "Mechanisms of fish damage in low head turbines: An experimental appraisal," *Fish migration and fish bypasses*, p. 300, 1998.

[49] A. Turnpenny, S. Clough, K. Hanson, R. Ramsay, and D. McEwan, *Risk assessment for fish passage through small, low-head turbines*. Atomic Energy Research Establishment, Energy Technology Support Unit, New and Renewable Energy Programme, 2000.

[50] R. J. Panton, *Incompressible Flow*. Hoboken, NJ: Wiley & Sons, 4th ed., 2013.

[51] D. Zhou, R. Roy, C.-Z. Wang, and J. Glahn, "Main gas ingestion in a turbine stage for three rim cavity configurations," *Journal of Turbomachinery*, vol. 133, no. 3, pp. 031023–031023–12, 2011.

[52] L. S. Sørensen, *An Introduction to Computational Fluid Dynamics: The Finite Volume Method*. Pearson, 2007.

[53] J. Vondál and J. Hájek, "Swirling flow prediction in model combustor with axial guide vane swirler," *Chemical Engineering*, vol. 29, no. 2, pp. 1069–1074, 2012.

[54] S. Galván, M. Reggio, and F. Guibault, "Numerical optimization of the inlet velocity profile ingested by the conical draft tube of a hydraulic turbine," *ASME J. Fluids Eng.*, vol. 137, no. 7, pp. 071102–071102–15, 2015.

[55] H. Ito, "Pressure losses in smooth pipe bends," *ASME J. Fluids Eng.*, vol. 82, no. 1, pp. 131–140, 1960.

[56] J. Nocedal and S. J. Wright, *Numerical Optimization*. New York: Springer, 2nd ed., 2006.

[57] A. Pumps, *1-1/2 inch Self-Priming Centrifugal Pumps Data Sheet*, 2016.

[58] M. Atilgan and J. Calvert, "Geometry of transition sections between ducts of equal area," *Journal of Wind Engineering and Industrial Aerodynamics*, vol. 6, no. 1, pp. 25–37, 1980.

[59] B. Munson, W. Huebsch, and A. Rothmayer, *Fundamentals of Fluid Mechanics*. Wiley, 2012.

[60] R. D. Mehta and P. Bradshaw, "Design rules for small low speed wind tunnels," *The Aeronautical Journal*, vol. 83, no. 827, pp. 443–453, 1979.

[61] E. Laws and J. Livesey, "Flow through screens," *Annual Review of Fluid Mechanics*, vol. 10, no. 1, pp. 247–266, 1978.

[62] J. Tan-Atichat, H. Nagib, and R. Loehrke, "Interaction of free-stream turbulence with screens and grids: a balance between turbulence scales," *Journal of Fluid Mechanics*, vol. 114, pp. 501–528, 1982.

[63] J. Scheiman, "Considerations for the installation of honeycomb and screens to reduce wind-tunnel turbulence," 1981.

[64] G. Morrison, J. Hauglie, and R. DeOtte, "Beta ratio, axisymmetric flow distortion and swirl effects upon orifice flow meters," *Flow Measurement and Instrumentation*, vol. 6, no. 3, pp. 207–216, 1995.

[65] W.-z. Ai and T.-m. Ding, "Orifice plate cavitation mechanism and its influencing factors," *Water Science and Engineering*, vol. 3, no. 3, pp. 321–330, 2010.

[66] MSE, *miniLDV brochure*, 2016.

[67] S. Tavoularis, *Measurement in fluid mechanics*. Cambridge University Press, 2005.

[68] J. L. Herrin and J. C. Dutton, "An investigation of LDV velocity bias correction techniques for high-speed separated flows," *Experiments in Fluids*, vol. 15, no. 4, pp. 354–363, 1993.

[69] J. L. Devore, *Probability and Statistics for Engineering and the Sciences*. Brooks/Cole Publishing Co., 2008.

[70] H. Vaidya, Ö. Ertunç, B. Genç, F. Beyer, Ç. Köksoy, and A. Delgado, "Numerical simulations of swirling pipe flows-decay of swirl and occurrence of vortex structures," in *Journal of Physics: Conference Series*, vol. 318, p. 062022, IOP Publishing, 2011.

[71] O. Kitoh, "Experimental study of turbulent swirling flow in a straight pipe," *Journal of Fluid Mechanics*, vol. 225, pp. 445–479, 1991.

APPENDICES

Appendix A

LDV beam diffraction

The refraction of the LDV beams causes the measured position to differ from the actual position. In order to rectify this, a geometric optical analysis was performed on the system. The following is a summary of the derivation procedure for the axial and circumferential velocity measurements.

A.0.1 Axial velocity measurements

One of the main equations in the analysis is Snell's law which is as follows.

$$n_1 \, sin\theta_i = n_2 \, sin\theta_t \tag{A.1}$$

Where n_1 and n_2 are the refraction coefficients of the two materials and θ_i and θ_t are the incident and transmitted angles.

The first incident angle $(\theta_{i,1})$ as the beam encounters the outer shell of the tube is the same as the incoming angle from the LDV. Using Snell's law, the transmitted angle $(\theta_{t,1})$ is obtained. The transmitted angle is then used as the incident angle $(\theta_{i,2})$ for the inner radius of the tube, which subsequently allows for the calculation of the final transmitted angle $(\theta_{t,2})$.

The normal vector for the point of incidence is defined as:

$$\hat{n}_1 = \hat{j} \tag{A.2}$$

The incoming (incident) beam vector is defined as:

$$\vec{b}_1 = b_1(-\cos(\theta_{i,1})\hat{j} - \sin(\theta_{i,1})\hat{k}) \tag{A.3}$$

Where b_1 is an arbitrary vector length. In order to constrain the transmission vector to the same plane as $\vec{b}_1$ and $\hat{n}_1$, the cross-product is taken between $\hat{n}_1$ and $\vec{b}_1$. This yields a vector normal to the plane $(\hat{n}_{p,1})$:

$$\vec{b}_1 \times \hat{n}_1 = \hat{n}_{p,1} = b_1\sin(\theta_{i,1})\hat{i} \tag{A.4}$$

Now that the plane has been defined, the transmitted vector $(\vec{b}_2)$ can be fully constrained and solved. The following 3 equations allow the vector to be fully constrained:

$$\vec{b}_1 \cdot \hat{n}_{p,1} = 0 \tag{A.5}$$

$$\vec{b}_1 \cdot \vec{b}_2 = |\vec{b}_1||\vec{b}_2|\cos(\theta_{i,1} - \theta_{t,1}) \tag{A.6}$$

$$\cos(\theta_{t,1}) = \frac{-\hat{n}_1 \cdot \vec{b}_2}{|\vec{b}_2|} \tag{A.7}$$

Equation A.5 forces $\vec{b}_2$ to be in the same plane as $\vec{b}_1$ and $\hat{n}_1$. Equations A.6 and A.7 constrain the angle between $\vec{b}_1$ and $\vec{b}_2$, and the angle between $\vec{b}_2$ and $\hat{n}_1$ respectively. Simultaneously solving the three equations above yields the components of $\vec{b}_2$, assuming that vector has a form $\vec{b}_2 = u_2\hat{i} + v_2\hat{j} + w_2\hat{k}$:

$$u_2 = 0 \tag{A.8}$$

$$v_2 = -cos(\theta_{t,1}) \tag{A.9}$$

$$w_2 = -\frac{1}{sin(\theta_{i,1})}(cos(\theta_{i,1} - \theta_{t,1}) - cos(\theta_{t,1})cos(\theta_{i,1})) \tag{A.10}$$

The magnitude of $\vec{b}_2$ can be obtained by using the transmitted angle $\theta_{t,1}$ and the thickness of the wall t:

$$b_2 = t\sqrt{1 + tan^2(\theta_{t,1})} \tag{A.11}$$

With $\vec{b}_2$ defined, the coordinates for the new point of incidence (i.e. y_2 and z_2 can be defined:

$$y_2 = y_1 + v_2 b_2 \tag{A.12}$$

$$z_2 = z_1 + w_2 b_2 \tag{A.13}$$

A similar process is used to determine $\vec{b}_3$, and subsequently point y_f which is where the refracted beams intersect. By compensating for the difference between the refracted location and the required location, the displacement can be corrected.

A.0.2 Circumferential velocity measurements

Vectors can be defined in order to locate the point at which the beam hits the surface of the cylinder. This point is defined by a vector ($\vec{R}$) which starts at the center of the cylinder and goes to the outer shell.

$$\vec{R} = R_1(cos(\theta_{xy})\hat{i} + sin(\theta_{xy})\hat{j}) \tag{A.14}$$

The vector's orientation is defined by an angle θ_{xy} which is a function of the y and x-coordinate. By setting up a virtual vector $(\vec{r^*})$ to where the location of the beam intersection is supposed to be and a vector defining the vector between the $\vec{r^*}$ and $\vec{R}$ $(\vec{r^{(1)}})$ and equating for length $r^{(1)}$, the angle θ_{xy} can be determined iteratively using Eq. A.17.

$$\vec{r^*} = y^*\hat{j} \tag{A.15}$$

$$\vec{r^{(1)}} = R_1(cos(\theta_{xy})\hat{i} + sin(\theta_{xy})\hat{j}) \tag{A.16}$$

$$R_1sin(\theta_{xy}) = \frac{R_1cos(\theta_{xy})}{tan(\theta_b)} + y^* \tag{A.17}$$

Where y^* is the desired location of the beam intersection, θ_b is the angle at which the LDV beam initial hits the outer cylinder surface. By defining vectors $\vec{b_1}$ and $\hat{n}_1$ as the incident vector of the beam and the vector normal to the surface of the outer cylinder and taking the dot product of the two vectors, the angle of incidence $\theta_{i,1}$ of the beam can be found.

$$\vec{b_1} = (cos(\theta_b)\hat{i} + sin(\theta_b)\hat{j}) \tag{A.18}$$

$$\hat{n}_1 = cos(\theta_{xy})\hat{i} + sin(\theta_{xy})\hat{j} \tag{A.19}$$

$$\theta_{i,1} = cos^{-1}\left(-cos(\theta_{xy})cos(\theta_b) + sin(\theta_{xy})cos(\theta_b)\right) \tag{A.20}$$

By defining $\hat{n}_{p,1}$ as the cross product of $\vec{b_1}$ and $\hat{n}_1$, the vector $\vec{b_2}$ can be constrained to the same plane as $\vec{b_1}$ and $\hat{n}_1$ by taking the dot product of $\hat{n}_{p,1}$ and $\vec{b_2}$ and making them equal to zero. This along with the constraint that the angle between $\vec{b_1}$ and $-\hat{n}_1$ is θ_{t1} and

that the angle between $\vec{b_1}$ and $\vec{b_2}$ is $\theta_{i,1} - \theta_{t,1}$ allows the coefficients of the vector $\vec{b_2}$ to be determined using simultaneous solutions. Assuming that $\vec{b_2}$ has the form $\vec{b_2} = b_2(u_2\hat{i} + v_2\hat{j})$, u_2 and v_2 are found:

$$u_2 = \frac{cos(\theta_b)cos(\theta_{t,1}) - cos(\theta_{i,1} - \theta_{t,1})sin(\theta_{xy})}{sin(\theta_b)sin(\theta_{xy}) - cos(\theta_b)cos(\theta_{xy})} \tag{A.21}$$

$$v_2 = \frac{-sin(\theta_b)cos(\theta_{t,1}) + cos(\theta_{i,1} - \theta_{t,1})cos(\theta_{xy})}{sin(\theta_b)sin(\theta_{xy}) - cos(\theta_b)cos(\theta_{xy})} \tag{A.22}$$

In order to find the magnitude of b_2, the angle relations in Fig. A.1 and Snell's law was used:

$$b_2 = R_1 \frac{sin(\beta)}{sin(\gamma)} \tag{A.23}$$

Similar to the axial deflection, the new coordinates for the point at which the beam hits the inner radius (i.e., x_2 and y_2) can now be calculated. A similar procedure is done when the beam reaches the inner radius of the outer cylinder. Through this, the actual location of the measuring volume can be determined. By interpolating for different values of y^*, the displacement can be corrected.
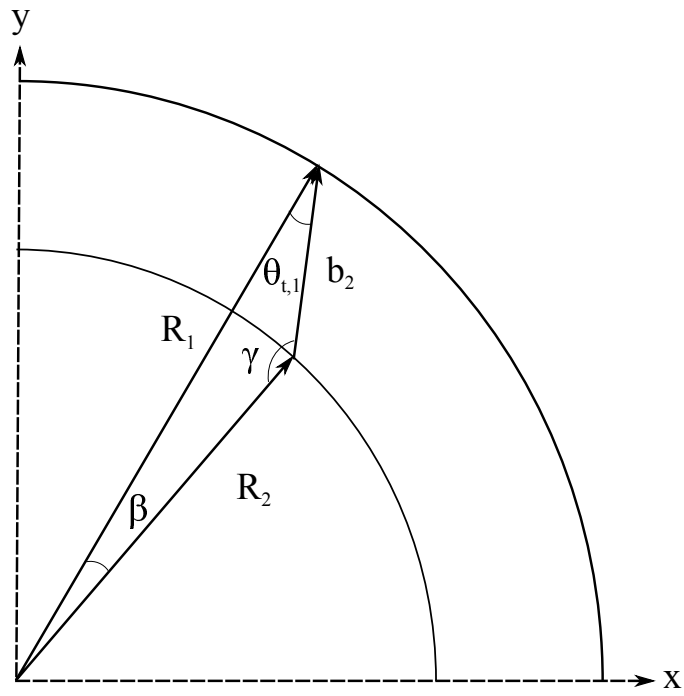
Figure A.1: Diagram illustrating the relationships between the different angles between the vectors.

Appendix B

Derivation of Euler turbine equation

The Euler turbomachine equation is used to calculate the power generated by the flow as it passes through the runner of the turbine or pump. The equation allows for a clear relationship between the flow characteristics and their effects on the performance of the turbomachine. In this particular study, the focus will be on the application of the Euler turbine equation on turbines.

The following is a derivation of the Euler turbine equation. Listed are the assumptions used in the derivation:

- Steady flow (i.e. $\dot{m}$ is constant).

- The circumferential velocity of the flow is the only component which does work.

- Momentum is conserved angularly.

- Axial velocity of the flow is constant.

The above assumptions are missing the losses that might be incurred due to friction. Furthermore, unsteady flow and axial compressibility of the flow are ignored.

The starting point of the derivation is the angular momentum equation:

$$\sum M_o = \frac{\partial}{\partial t} \left[\int_{CV} (\vec{r} \times \vec{v})\rho \, dV \right] + \int_{CS} (\vec{r} \times \vec{v})\rho(\vec{v} \cdot \vec{n}) \, dA \tag{B.1}$$

$$\sum M_o = \sum (\vec{r} \times \vec{v})_{out} \dot{m}_{out} - \sum (\vec{r} \times \vec{v})_{in} \dot{m}_{in} \tag{B.2}$$

$$\tau = r_{out} v_{out} \dot{m}_{out} - r_{in} v_{in} \dot{m}_{in} \tag{B.3}$$

In an axial turbine with a constant diameter, $r = r_{in} = r_{out}$ and by conservation of mass, $\dot{m} = \dot{m}_{in} = \dot{m}_{out}$. Therefore the above equation becomes:

$$\tau = r\dot{m}(v_{out} - v_{in}) \tag{B.4}$$

The total torque is the difference between the momentum of the fluid at the inlet and outlet. Since the only the circumferential component of velocity is generating work the torque formula becomes the following:

$$\tau = r\dot{m}(C_{w2} - C_{w1}) \tag{B.5}$$

The subscript 1 defines the inlet and subscript 2 defines the outlet. The power can subsequently be derived as a function of the torque and the shaft speed:

$$P = \tau \Omega = \dot{m} U (C_{w2} - C_{w1}) \tag{B.6}$$

Where $U = \Omega r$.

By dividing the power by the mass flow rate the work can obtained for the stage:

$$W = \frac{P}{\dot{m}} = U(C_{w2} - C_{w1}) \tag{B.7}$$

Depending on whether the work is positive or negative, the formula for either a compressor or a turbine can be obtained. When $W > 0$ then then the Euler Pump Equation is obtained. When $W < 0$ then then the Euler Turbine Equation is obtained.

Therefore the Euler Turbine Equation is as follows:

$$W = U(C_{w1} - C_{w2}) \tag{B.8}$$

The equation can be re-written into a energy for by using the relationship between the velocities as shown in Fig. B.1.
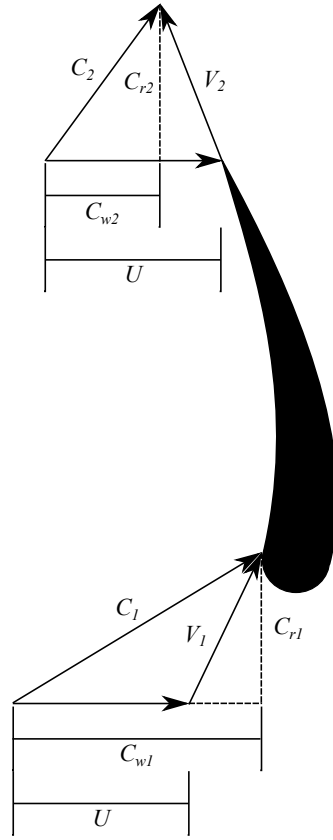
Figure B.1: Velocity triangles for the flow through a turbine.

From the triangle, the following relationships can be found:

$$C_1^2 = C_{r1}^2 + C_{w1}^2 \tag{B.9}$$

$$V_1^2 = C_{r1}^2 + (U - C_{w1})^2 \tag{B.10}$$

By isolating for C_{r1}^2 and substituting into Eq. B.10 ,the following relationship can be found:

$$UC_{w1} = \frac{C_1^2 + U^2 - V_1^2}{2} \tag{B.11}$$

94

Similarly for the outlet:

$$UC_{w2} = \frac{C_2^2 + U^2 - V_2^2}{2} \tag{B.12}$$

By replacing the above terms in the Euler Turbine Equation, it can be written as:

$$W = U(C_{w1} - C_{w2}) = \frac{(C_1^2 - C_2^2) + (V_2^2 - V_1^2)}{2} \tag{B.13}$$

Where $\frac{(C_1^2 - C_2^2)}{2}$ is the change of absolute kinetic energy of the fluid and $\frac{(V_1^2 - V_2^2)}{2}$ is the change of kinetic energy due to the change in relative velocity of fluid. In cases where the radius is not uniform from inlet to exit, there is an extra component, $\frac{(U_1^2 - U_2^2)}{2}$, which is the change of centrifugal head energy of the fluid.